

Theoretical study of photonic band gaps in woodpile crystals

Boris Gralak* and Michiel de Dood†

FOM-Institute for Atomic and Molecular Physics, Kruislaan 407, 1098 SJ Amsterdam, The Netherlands

G rard Tayeb,‡ Stefan Enoch, and Daniel Maystre

Institut Fresnel (UMR 6133), Facult  des Sciences et Techniques de St. J r me, case 161, 13397 Marseille Cedex 20, France

(Received 21 January 2003; published 4 June 2003)

We investigate numerically the existence of photonic band gaps in woodpile crystals. We present a numerical method specifically developed to solve Maxwell's equations in such photonic structures. It is based upon a rigorous mathematical formulation and leads to a considerable improvement of the convergence speed as compared to other existing numerical methods. We tested our method by comparing the calculated reflectivity with measurements on an actual sample, i.e., a silicon woodpile photonic crystal designed for $1.5 \mu\text{m}$ wavelength. Excellent agreement is obtained, provided the main structural imperfections of the sample are taken into account. We show that the existence of photonic band gaps in woodpile crystals requires an index contrast higher than 2.05 ± 0.01 . The effects of imperfections of such structures with an index contrast equal to 2.25 are also investigated. Thus, the relative band gap width falls from 3.5% to 2.2% with structural imperfection similar to those of the sample.

DOI: 10.1103/PhysRevE.67.066601

PACS number(s): 42.70.Qs, 42.25.Bs

I. INTRODUCTION

The main motivation for studying photonic crystals is their possible ability to inhibit spontaneous photon emission [1,2]. This is a consequence of the existence of photonic band gaps [3,4], i.e., frequency intervals, where the propagation of the electromagnetic field is forbidden, whatever the polarization and the propagation direction. Indeed, it is expected that an excited atom, embedded in a photonic crystal, cannot radiate if the atomic transition frequency falls in a photonic band gap since the electromagnetic energy cannot propagate away [2]. In addition to these physical arguments, rigorous theoretical studies [5,6] showed that the single-photon decay rate is proportional to the local density of states. Since this local density of states vanishes in a photonic band gap, these theoretical studies confirm the possibility for inhibiting spontaneous emission.

The existence of a photonic band gap is the result of a periodic modulation, together with sufficient contrast of the permittivity (we refer to its square root as the index). From the experimental side, the main difficulty is to realize three-dimensional periodic structures having a reasonable accuracy in the periodicity, combined with a sufficiently high permittivity contrast in the optical or infrared regime. At present it is thought that the most promising current experimental realizations are face-centered-cubic lattices of microspheres realized using colloid techniques [7,8] as inverted opals [9,10], and woodpile structures [11–13].

Using a suitably adapted Korringa-Kohn-Rostocker method [14], it has been shown that an index contrast higher than 2.85 [15] is required to create a photonic band gap in face-centered-cubic lattices of microspheres. Thus, transpar-

ent dielectric materials are prohibited in the optical range. This is why microspheres made of metals or semiconductors have been considered. A numerical study showed the existence of a wide photonic band gap for the optical range if absorption is neglected [16]. However, a quantitative estimate of the effects of absorption remains necessary since spontaneous emission cannot be strictly inhibited in the presence of absorption [17]. On the other hand, the concept of local density of states can be generalized to absorptive materials [18], it determines whether or not absorption is negligible.

We consider in this paper, the second type of promising structures, woodpile crystals. The latter have been studied intensively by numerical methods, using an expansion of the electromagnetic field and the permittivity into the Fourier (or plane-waves) basis. This expansion was used to predict photonic band gap edges [19], the effect of several structural imperfections on such edges [20], the decay rate for single-photon emission in infinite structures [21] and reflectivity and the inhibition of spontaneous emission for finite-thickness structures [22]. However, the use of a plane-wave expansion leads to poor convergence, due to the discontinuous nature of both the electromagnetic field and the permittivity [23]. For this reason, we have developed a numerical method well adapted to woodpile structures. Here, the electromagnetic field is expanded using an "exact eigenfunctions basis" for which an exact representation of the permittivity is available [24–26].

Since this paper covers a broad field (from a mathematical formulation to an experimental comparison), we present in Sec. II a summary of the most important ideas and results. Next, in Sec. III, we give a self-consistent presentation of the numerical method we have developed. In particular, we discuss the underlying mathematical formalism. Then, in Sec. IV, we verify our method by performing a convergence test and by checking energy conservation. In addition, we compare in Sec. IV C the directly calculated reflectivity curves

*Electronic address: gralak@amolf.nl

†Electronic address: mdedood@physics.ucsb.edu

‡Electronic address: gerard.tayeb@fresnel.fr

with experimentally measured data on a silicon woodpile photonic crystal designed for a wavelength of $1.5 \mu\text{m}$ [12]. Here, we benefit from the efficiency of the method, which permits us to take into account the structural imperfections of the sample and the frequency dependence of the silicon permittivity. These results complement our previous study of this experimental setup, presented in Ref. [27]. Finally, in Sec. V, we study the existence of photonic band gaps in woodpile devices. Thus, we conclude that it is possible to construct woodpile structures with photonic band gaps, using ordinary materials, transparent in the optical range and, as a consequence, that it is possible to suppress spontaneous emission in the optical regime.

II. STATEMENT OF THE MAIN RESULTS

A. The numerical method

We show here that our method is better adapted to the case of woodpile structures than the plane-wave method [28–30], the Korringa-Kohn-Rostocker (KKR) method [14] and the method based on the scattering matrix [22,31].

1. Existing numerical methods

The plane-wave method [28–30] is the most frequently used numerical method for photonic crystals and, in particular, for woodpile devices. It involves an expansion in the Fourier (or plane-waves) basis for the electromagnetic field and the permittivity in the three space directions. Recall that if \mathcal{M} is the number of Fourier coefficients used to expand a periodic function in one space direction, then the total number of plane-waves growth with $\mathcal{N}=\mathcal{M}^3$. The electromagnetic field and the permittivity being discontinuous, convergence is poor and \mathcal{N} must be very high (more than $7\times 7\times 7$ for an error of only a few percent [23,32]), leading to considerable calculation time. Moreover, this method cannot handle frequency dependent or complex permittivities and, in addition, does not provide quantities associated with finite-size structures (such as reflectivity or emitted power by embedded atoms) which can be compared to experimental measurement.

The KKR method, adapted to Maxwell’s equations [14], gives a solution to many problems encountered with the plane-wave method. Convergence is fast (it requires about 3×3 spherical waves, while the plane-wave method requires $7\times 7\times 7$ plane waves) and it can deal with frequency dependent and complex permittivity [16,33]. Moreover, in tandem with results about sums of spherical waves for two-dimensional lattices [34], this method makes it possible to solve Maxwell’s equations for finite-width structures [35]. However, the KKR method, with its emphasis on spherical or cylindrical symmetry, is poorly adapted to woodpile crystals.

The most efficient method currently used for the study of woodpile structures is, to our knowledge, based on the scattering matrix [22,31]. Indeed, this method can deal with frequency dependent and complex permittivities and can deal with quantities associated with finite-thickness structures [31]. Moreover, the plane-wave expansion is only used in two directions of the real space, while Maxwell’s equations

are solved in the third direction [31]. Instead of being proportional to \mathcal{M}^3 now $\mathcal{N}=\mathcal{M}^2$ (and the typical required number of plane waves is 7×7 to obtain a 1% error for the first band [22]).

2. The new numerical method

Our numerical method is similar to the one based on the scattering matrix [22,31] (and hence has the same characteristics), but with two fundamental improvements. The first is a consequence of the stable algorithm presented in a previous paper [36]. Using the sophisticated techniques used for gratings in Ref. [37], the latter has the feature to solve Maxwell’s equations without numerical instabilities for both the infinite- (in three space direction) and finite-thickness (i.e., infinite in two space directions) cases. Thus, we refer to our general numerical framework as the “grating method.” The second improvement relies on a generalization of the method of “exact eigenvalues and eigenfunctions” employed in the study of lamellar grating [24,26].

The “grating method” consists in first solving Maxwell’s equations for a finite-thickness photonic crystal (or a grating), and then imposing boundary conditions at the boundaries of the top and the bottom planes which delimit this grating. We now denote any quantity that is contained in these planes by tangential. By imposing different boundary conditions, we are able to estimate different quantities from a single numerical code.

(1) The outgoing wave condition [31,37] gives the reflectivity and the transmittance.

(2) The “point current source” condition [31,38] gives the Green’s function (i.e., the electromagnetic field radiated by a point current source and then the local density of states).

(3) The Bloch boundary condition [36] gives the dispersion relation and other quantities for infinite structures in three space directions. We think that imposing this condition without numerical instabilities is a fundamental improvement since it allows convergence tests that ensure the accuracy of the results.

Moreover, the stable algorithm can provide a very important reduction of calculation time. Indeed, for a given frequency and two tangential components of the Bloch wave vector, the algorithm provides all the third components of the latter. The Brillouin zone is then reduced to its projection onto the tangential components plane (a volume is reduced to a surface in the three-dimensional case and a surface is reduced to a line in the two-dimensional case).

The second improvement consists in benefiting from all the sophisticated techniques developed in the numerical study of gratings [37]. The numerous techniques developed in the study of gratings are now mature since the stable S and R algorithms [39] of continuation into the third direction have been established and since the convergence of the Fourier series has been systematically improved [40] when they are used. Among these available numerous techniques, we mention the efficient integral [41] and differential [42,43] methods that allow one to solve general problems. We also mention the modal method [44,45] that takes advantage of the piecewise invariance in the third direction of the permittivity (this modal method is a generalization of the method

based on the scattering matrix presented in Ref. [31]). For woodpile structures, we have generalized the method of exact eigenvalues and eigenfunctions in order to take advantage of the single variable dependence of the permittivity in each layer.

The method of exact eigenvalues and eigenfunctions has been developed for the numerical study of lamellar gratings [24]. Taking advantage of the geometry, the electromagnetic field is expanded on a suitable basis and the permittivity is exactly represented. Since these pioneering works, the main contribution to this method is certainly its rigorous extension to conical mountings [26]. This extension gives the possibility to generalize this method to woodpile structures and then to benefit of its advantages. The fast convergence speed observed for the lamellar grating is also found for woodpile structures, leading to a very important reduction of calculation time: the method requires $\mathcal{N} = \mathcal{M}^2 = 3 \times 3$ of basis functions for an error around 1% for frequencies corresponding to the first band number, while 7×7 plane waves are required provided the most efficient existing method [22] is used. This improvement is very useful since it allows us to consider more complicated structures that are closer to the experimental realizations.

B. Results

1. The mathematical formulation

The first result of the mathematical formulation is that, in each layer, there is a decoupling of the vector field equations into two independent scalar equations. Our second result is the introduction of a continuation procedure, permitting us to solve an elliptic evolution equation. With these results, we obtain an expression for Maxwell's equations for woodpile structures in terms of simple scalar operators and it is possible to determine the eigenvalues and the eigenfunctions of these operators exactly.

2. Experimental verification of the numerical method

In this paper, we compare our numerical results with the experimental measurements of the reflectivity on silicon woodpile photonic crystal [12] for wavelengths ranging from $1.0 \mu\text{m}$ to $1.7 \mu\text{m}$.

The comparison shows good agreement for the upper band gap edge and for the reflectivity for frequencies in the gap (the difference is always smaller than several percents) except for a deep peak in the band gap in the experiment. We show that this peak is not the consequence of dispersion in silicon (indeed, the effect of silicon dispersion can be neglected since the frequency dependence of the permittivity is quite small in the considered frequency range) but of a structural imperfection of the experimental setup. A scanning electron microscope image [27] shows that every other silicon rod which constitute the woodpile crystal is slightly shifted as mentioned in Ref. [12]. Taking into account this structural imperfection, very good agreement is obtained for the position, width, and depth of the peak. Finally, as reported in Ref. [27], the theoretical explanation of this peak is due to the fact that the structural imperfections lead to a

woodpile crystal with tangential spatial periods twice the original ones.

However, the comparison shows significant differences between the theoretical results and the experimental measurements of the reflectivity for wavelengths outside the band gap, even if we take into account the silicon dispersion and (or) the structural imperfections described above. We conclude that, in this wavelength range, the many slight fluctuations of the structure lead to important perturbations which blur the effect of the periodic arrangement.

3. Numerical study of photonic band gaps in woodpile structures

We investigate the relative band gap width in face-centered-cubic woodpile crystals similar to the experimental devices [11–13]. A unit cell of these face-centered-cubic lattices consists of a dielectric background surrounding two identical, perpendicular, nonoverlapping, and contiguous dielectric rods with rectangular cross section. The relevant parameters are then the filling ratio (the ratio of the rod width and the unit cell width) and the index contrast (the ratio of the dielectric rod's index and the background's index). Varying these parameters, we found that the minimal index contrast required to open a band gap is equal to 2.05 ± 0.01 (a filling ratio equal to 0.43 ± 0.01 is then required). Note that we made convergence tests to ensure the accuracy of the result.

Finally, we consider a woodpile crystal with a relatively low index contrast, equal to 2.25, which can correspond to an ordinary transparent material (such as Ta_2O_5) and air in the optical range. We show that, in this case, the relative band gap width is equal to $3.5\% \pm 0.1\%$ for the optimal filling ratio, equal to 0.38 ± 0.02 . Taking into account a structural imperfection similar to the one of the actual silicon woodpile crystal [12] considered in the experimental validation of the method, we show that a band gap still opens for a deviation as far as 18% of the unit cell width. In particular, for a deviation of 10% of the unit cell width (this deviation is similar to the one of the considered experimental silicon woodpile crystal), the relative band gap width is equal to $2.2\% \pm 0.1\%$.

III. THE METHOD OF “EXACT EIGENVALUES AND EIGENFUNCTIONS”

In this section, we give a self-consistent presentation of the extension to woodpile structures of the method of exact eigenvalues and eigenfunctions derived for the gratings in conical mountings in Ref. [26]. We show how to obtain in the presence of woodpile structures a large class of solutions E_ω of the Helmholtz equation

$$[\omega^2 - \varepsilon^{-1} \nabla \times \mu^{-1} \nabla \times] E_\omega = \mathbf{0}, \quad (1)$$

where ε is the permittivity, μ is the permeability, and ω is the frequency. For the sake of simplicity, we only consider real frequency and real, strictly positive and bounded, permittivity and permeability since the generalization to any complex valued functions does not differ from the one given in Ref. [26]:

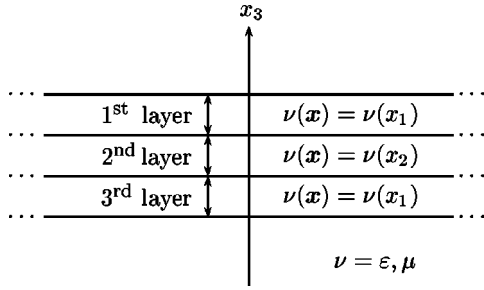


FIG. 1. A woodpile structure made of three stacked layers.

$$\omega \in \mathbb{R}, \quad 0 < \varepsilon_- \leq \varepsilon \leq \varepsilon_+, \quad 0 < \mu_- \leq \mu \leq \mu_+, \quad (2)$$

where ε_- , ε_+ , μ_- , and μ_+ are positive real numbers.

A. Notations

1. Geometry

Throughout this paper, we use an orthonormal basis $(\mathbf{e}_1, \mathbf{e}_2, \mathbf{e}_3)$: every vector \mathbf{x} in \mathbb{R}^3 is described by its three components x_1 , x_2 , and x_3 . The structure we consider is periodic in two directions with spatial periods $\mathbf{d}_1 = d_{1,1}\mathbf{e}_1$ and $\mathbf{d}_2 = d_{2,2}\mathbf{e}_2$:

$$\nu(\mathbf{x} + \mathbf{d}_j) = \nu(\mathbf{x}), \quad \mathbf{x} \in \mathbb{R}^3, \quad (3)$$

where $\nu = \varepsilon, \mu$, and $j = 1, 2$. The unit cell of the two-dimensional lattice associated with this structure is

$$V = \{\mathbf{x} = a_1\mathbf{d}_1 + a_2\mathbf{d}_2 \mid a_1, a_2 \in [-1/2, 1/2]\}. \quad (4)$$

Then, a woodpile structure is a stack in the third direction of layers, where ε and μ are functions dependent on a single variable, the latter being x_1 or x_2 (Fig. 1). In practice, each layer is made up from infinite parallel rods with rectangular cross section (Fig. 2). Thus, the functions ε and μ are piecewise constant.

2. Electromagnetic field

In order to obtain a set of first-order differential equations from Eq. (1), we define

$$\mathbf{H}_\omega = (\omega\mu)^{-1}\nabla \times \mathbf{E}_\omega. \quad (5)$$

Note that this quantity differs from the usual ‘‘harmonic \mathbf{H} field’’ by the complex number i .

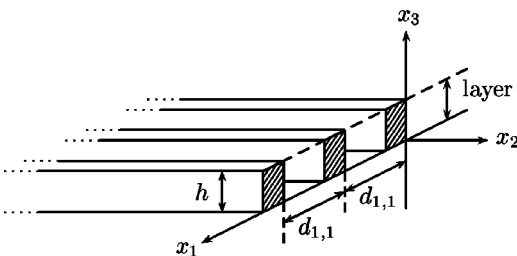


FIG. 2. A layer made of two rods per unit cell; ε and μ are piecewise constant and periodic functions of the single variable x_1 . The thickness of the layer is h .

We investigate solutions \mathbf{E}_ω , \mathbf{H}_ω , whose restrictions in every horizontal plane (normal to \mathbf{e}_3) are square integrable:

$$\int_{\mathbb{R}^2} |\mathbf{F}_\omega(x_1, x_2, x_3)|^2 dx_1 dx_2 < \infty, \quad x_3 \in \mathbb{R}, \quad (6)$$

where $\mathbf{F}_\omega = \mathbf{E}_\omega, \mathbf{H}_\omega$.

The first consequence of Eq. (6) is the possibility to perform a Floquet-Bloch decomposition associated with the two-dimensional periodicity (3). Thus, we investigate solutions \mathbf{E} , \mathbf{H} that satisfy

$$\int_V |\mathbf{F}(x_1, x_2, x_3)|^2 dx_1 dx_2 < \infty, \quad x_3 \in \mathbb{R}, \quad (7)$$

with the partial Bloch boundary condition

$$\mathbf{F}(\mathbf{x} + \mathbf{d}_j) = \exp(2i\pi k_j)\mathbf{F}(\mathbf{x}), \quad \mathbf{x} \in \mathbb{R}^3, \quad (8)$$

where (k_1, k_2) is fixed in $[-1/2, 1/2]^2$, $\mathbf{F} = \mathbf{E}, \mathbf{H}$, and $j = 1, 2$. Note that for the symbols \mathbf{E} and \mathbf{H} , we have omitted the fixed parameters ω , k_1 , and k_2 in order to clarify the further calculations.

The second consequence of Eq. (6) [or Eq. (7)] is that the restrictions to every horizontal plane of $\nabla \times \mathbf{E}$ and $\nabla \times \mathbf{H}$ are locally square integrable as well [from Eqs. (1), (2), and (5)]. Then, for all $i, j = 1, 2, 3$ and $i \neq j$, E_i and H_i are continuous functions of the variable x_j . In particular, the tangential components E_1 , E_2 , H_1 , and H_2 of \mathbf{E} and \mathbf{H} are continuous functions of the variable x_3 . It follows that it is possible to solve Maxwell’s equations in a stack of layers by the following two steps: the first step consists in solving Maxwell’s equations in each layer independently and then the second step consists in connecting each independent solution using the continuity of E_1 , E_2 , H_1 , and H_2 .

B. The mathematical formulation

In the following Secs. III B 1, III B 2, and III B 3, we consider a single layer of rods bounded by the horizontal planes defined by the equations $x_3 = 0$ and $x_3 = h$ (Fig. 2), where ε and μ are functions of the variable x_1 only (the case where ε and μ depend on x_2 is similar):

$$0 \leq x_3 \leq h \Rightarrow \varepsilon(\mathbf{x}) = \varepsilon_1(x_1), \quad \mu(\mathbf{x}) = \mu_1(x_1). \quad (9)$$

1. Decoupling of the field in a layer

With definition (5) and notation (9), Eq. (1) is equivalent to the set of first-order equations

$$\mathbf{E} = (\omega\varepsilon_1)^{-1}\nabla \times \mathbf{H}, \quad \mathbf{H} = (\omega\mu_1)^{-1}\nabla \times \mathbf{E}, \quad (10)$$

in the considered layer. After eliminating the vertical components E_3 and H_3 , one obtains the equation

$$\partial_3 \begin{bmatrix} F_1 \\ F_2 \end{bmatrix} = \begin{bmatrix} -\partial_1 \sigma_1^{-1} \partial_2 & \sigma_1 + \partial_1 \sigma_1^{-1} \partial_1 \\ -\sigma_1 - \partial_2 \sigma_1^{-1} \partial_2 & \partial_2 \sigma_1^{-1} \partial_1 \end{bmatrix} \begin{bmatrix} F_1 \\ F_2 \end{bmatrix}, \quad (11)$$

where ∂_j is the partial derivative with respect to the variable x_j ($j = 1, 2, 3$) and

$$\sigma_1 = \omega \begin{bmatrix} 0 & \varepsilon_1 \\ \mu_1 & 0 \end{bmatrix}, \quad F_j = \begin{bmatrix} E_j \\ H_j \end{bmatrix}, \quad j=1,2. \quad (12)$$

Since the functions ε_1 and μ_1 (and then the matrix σ_1) are x_3 independent in a single layer, Eq. (11) implies that

$$\partial_3^2 \begin{bmatrix} F_1 \\ F_2 \end{bmatrix} = \begin{bmatrix} -\sigma_1^2 - \partial_1 \sigma_1^{-1} \partial_1 \sigma_1 - \sigma_1 \partial_2 \sigma_1^{-1} \partial_2 & \sigma_1 \partial_2 \sigma_1^{-1} \partial_1 - \partial_1 \sigma_1^{-1} \partial_2 \sigma_1 \\ \sigma_1 \partial_1 \sigma_1^{-1} \partial_2 - \partial_2 \sigma_1^{-1} \partial_1 \sigma_1 & -\sigma_1^2 - \partial_2 \sigma_1^{-1} \partial_2 \sigma_1 - \sigma_1 \partial_1 \sigma_1^{-1} \partial_1 \end{bmatrix} \begin{bmatrix} F_1 \\ F_2 \end{bmatrix}. \quad (13)$$

Since the matrix σ_1 is x_2 independent in the considered layer, we have $\sigma_1^{-1} \partial_2 \sigma_1 = \partial_2 = \sigma_1 \partial_2 \sigma_1^{-1}$, so from the last equation,

$$\partial_3^2 F_1 = -L_1 F_1, \quad L_1 = \begin{bmatrix} L_{\mu_1} & 0 \\ 0 & L_{\varepsilon_1} \end{bmatrix}, \quad (14)$$

where

$$L_{\nu_1} = \omega^2 \varepsilon_1 \mu_1 + \partial_1 \nu_1^{-1} \partial_1 \nu_1 + \partial_2^2, \quad \nu_1 = \varepsilon_1, \mu_1. \quad (15)$$

Solving Eq. (14) will provide the vectors F_1 and its first derivative $\partial_3 F_1$. Moreover, from Eq. (11), the vectors F_1 , F_2 , and $\partial_3 F_1$ are related. Maxwell's equations are then reduced to Eq. (14), which can be considered as two scalar and independent equations for the components E_1 and H_1 . This remarkable phenomenon of decoupling of the field in a three-dimensional structure makes the solution easier on both the mathematical and numerical sides.

2. Continuation of the field in the third direction

In this section, we solve Eq. (14) using a suitable continuation procedure. In order to clarify the calculations of this section, we rewrite this equation as the evolution equation

$$\frac{d^2 \psi}{dt^2}(t) = -L_1 \psi(t), \quad (16)$$

in the Hilbert space $\mathcal{H}_1 = \mathcal{H}_{\mu_1} \oplus \mathcal{H}_{\varepsilon_1}$, where $\mathcal{H}_{\nu_1} = L_{k_1, k_2}^2(V, \nu_1 dx_1 dx_2; \mathbb{C})$ is the set of locally square integrable and complex valued functions with the boundary condition (8) and the inner product $\langle \cdot, \cdot \rangle_{\nu_1}$:

$$\phi, \phi' \mapsto \frac{1}{|V|} \int_V \overline{\phi(x_1, x_2)} \phi'(x_1, x_2) \nu_1(x_1) dx_1 dx_2, \quad (17)$$

where $|V| = d_{1,1} d_{2,2}$ and $\nu_1 = \varepsilon_1, \mu_1$. First, we remark that L_1 defines a self-adjoint operator in \mathcal{H}_1 . Indeed, it is easy to verify that L_1 is a symmetric and semibounded operator [$L_1 \leq \omega^2 \varepsilon_+ \mu_+$ from Eqs. (2), (14), and (15)]: the self-adjointness can be shown by quadratic form techniques [46]. Since L_1 is not a positive operator, we cannot use the usual continuation procedure [47,48] to solve the Eq. (14). On the numerical side, this problem emerges with the instabilities of the transfer matrix. However, suitable numerical continua-

tion algorithms [39] that permit to solve equations similar to Eq. (14) have been developed. So, inspired by these numerical algorithms, we will define a suitable continuation procedure.

We define for all λ in $(-\infty, \omega^2 \varepsilon_+ \mu_+]$ and for all s, t such that $0 \leq |t| \leq |s| \leq h/2 < \pi/(4\omega \sqrt{\varepsilon_+ \mu_+})$ two real valued functions $f_{t,s}$ and $g_{t,s}$ given by

$$f_{t,s}(\lambda) = \frac{\cos[\sqrt{\lambda}(t+s)]}{\cos[\sqrt{\lambda}2s]}, \quad (18a)$$

$$g_{t,s}(\lambda) = \frac{\sin[\sqrt{\lambda}(t-s)]}{\sqrt{\lambda} \cos[\sqrt{\lambda}2s]}. \quad (18b)$$

Note that $\cos(\sqrt{\lambda})$ and $\sin(\sqrt{\lambda})/\sqrt{\lambda}$ can be expressed as a power series in λ and that functions $f_{t,s}$ and $g_{t,s}$ are uniformly bounded (with respect to s, t , and λ) by $1/\cos(h\omega \sqrt{\varepsilon_+ \mu_+})$. Since L_1 is self-adjoint and semi-bounded, we can define, by the functional calculus [46], the operators $f_{t,s}(L_1)$ and $g_{t,s}(L_1)$ which are self-adjoint and uniformly bounded. Now, we can define the propagator

$$R(t,s) = \begin{bmatrix} f_{t,s}(L_1) & -g_{t,s}(L_1) \\ -L_1 g_{t,s}(L_1) & f_{t,s}(L_1) \end{bmatrix}, \quad (19)$$

which has the usual properties of propagators [47] and, which satisfies

$$\frac{dR}{dt}(t,s) = - \begin{bmatrix} 0 & 1 \\ L_1 & 0 \end{bmatrix} R(-t,s), \quad (20)$$

since $f_{t,s}$ and $g_{t,s}$ are infinitely differentiable with respect to t (and s). Finally, if we define

$$\Psi(t) = R(t,s) \Psi(s), \quad \Psi(t) = \begin{bmatrix} \psi(-t) \\ (d\psi/dt)(t) \end{bmatrix}, \quad (21)$$

then the combination of Eqs. (20) and (21) shows that $\psi(t)$ satisfies Eq. (16) for all t in $[-|s|, |s|]$. In particular, taking Eq. (21) with $s = -h/2$ and $t = h/2$, one obtains the relationship $\Psi(h/2) = R(h/2, -h/2) \Psi(-h/2)$, i.e., a relationship between the values of ψ and $d\psi/dt$ at the boundaries of a layer of thickness h (Fig. 2). Note that the propagator $R(h/2, -h/2)$ is similar to the R matrix used in the R algorithm [39].

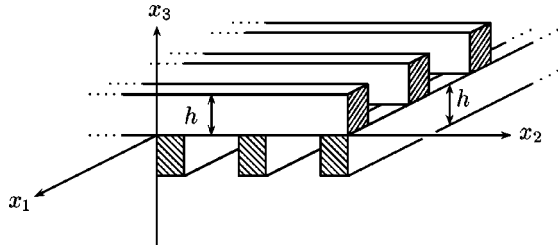


FIG. 3. The “superlayer” of a simple woodpile crystal. This superlayer is made of two layers that are identical after a rotation of 90° of one of them.

3. Solution of Maxwell's equations in a layer

We continue the calculations of Sec. III B 1. Since the equations are considered in the Hilbert space \mathcal{H}_1 , $F_j(\cdot, \cdot, x_3)$ and $(\partial_3 F_j)(\cdot, \cdot, x_3)$ are, respectively, denoted by $F_j(x_3)$ and $(\partial_3 F_j)(x_3)$, $j=1,2$. From relation (21) the values of F_1 and $\partial_3 F_1$ at the planes (defined by $x_3=0$ and $x_3=h$) bounding the considered layer of thickness h are related by

$$\begin{bmatrix} F_1(0) \\ (\partial_3 F_1)(0) \end{bmatrix} = R(h/2, -h/2) \begin{bmatrix} F_1(h) \\ (\partial_3 F_1)(h) \end{bmatrix}. \quad (22)$$

Finally, using that, from Eq. (11), $(\partial_3 F_1)(x_3) = (L_1 - \partial_2^2) \sigma_1^{-1} F_2(x_3) - \partial_1 \sigma_1^{-1} \partial_2 F_1(x_3)$, we obtain the following relation for the tangential components of the field:

$$M_1(h) \begin{bmatrix} F_1(0) \\ F_1(h) \end{bmatrix} = N_1(h) \begin{bmatrix} \sigma_1^{-1} F_2(0) \\ \sigma_1^{-1} F_2(h) \end{bmatrix}, \quad (23)$$

where, denoting $f_{-h/2, h/2}$ and $g_{-h/2, h/2}$, respectively, by f_h and g_h ,

$$M_1(h) = \begin{bmatrix} 1 - g_h(L_1) \partial_1 \sigma_1^{-1} \partial_2 & f_h(L_1) \\ f_h(L_1) \partial_1 \sigma_1^{-1} \partial_2 & L_1 g_h(L_1) - \partial_1 \sigma_1^{-1} \partial_2 \end{bmatrix},$$

$$N_1(h) = \begin{bmatrix} -g_h(L_1)(L_1 - \partial_2^2) & 0 \\ f_h(L_1)(L_1 - \partial_2^2) & -(L_1 - \partial_2^2) \end{bmatrix}. \quad (24)$$

Relation (23) gives the general solution of Maxwell's equations in a layer of thickness $h < \pi/(2\omega\sqrt{\varepsilon_+ \mu_+})$. Note that this limitation on h is introduced to ensure the absence of a division by zero in definition (18) of functions $f_{t,s}$ and $g_{t,s}$. Without this limitation, a discontinuity could appear in propagator (19) leading to the impossibility for the continuation of the field. Finally, when the layer thickness h exceeds the value $\pi/(2\omega\sqrt{\varepsilon_+ \mu_+})$, a solution can be found by dividing the layer into “sublayers” of sufficiently small thickness.

4. Bloch solution of Maxwell's equations in a woodpile crystal

In this section, we consider a simple woodpile crystal consisting of an infinite stack of identical “superlayers,” each “superlayer” consisting of a stack of a top and a bottom layer (Fig. 3).

These two layers are identical after a rotation of 90° of one of them. Now, suppose that the top layer is similar to the

one considered in Secs. III B 1, III B 2, and III B 3. Then, the bottom layer is delimited by the planes defined by equations $x_3 = -h$ and $x_3 = 0$ (Fig. 3), and functions ε and μ satisfy

$$-h \leq x_3 \leq 0 \Rightarrow \varepsilon(\mathbf{x}) = \varepsilon_2(x_2), \quad \mu(\mathbf{x}) = \mu_2(x_2), \quad (25)$$

where $\varepsilon_2(t) = \varepsilon_1(t)$ and $\mu_2(t) = \mu_1(t)$ for all real t since the two layers are identical. We denote by σ_2 the associated matrix that is analogous to the matrix σ_1 (12), and by

$$L_2 = \sigma_2^2 + \partial_2 \sigma_2^{-1} \partial_2 \sigma_2 + \partial_1^2 \quad (26)$$

the operator associated with the bottom layer which is analogous to the operator L_1 (14) and (15). L_2 defines a self-adjoint operator in the Hilbert space $\mathcal{H}_2 = \mathcal{H}_{\mu_2} \oplus \mathcal{H}_{\varepsilon_2}$, where $\mathcal{H}_{\nu_2} = L_{k_1, k_2}^2(V, \nu_2 dx_1 dx_2; \mathbb{C})$, $\nu_2 = \varepsilon_2, \mu_2$.

The general solution of Maxwell's equations in the top layer satisfies (23) and, from a similar reasoning, the general solution of Maxwell's equations in the bottom layer satisfies

$$M_2(h) \begin{bmatrix} F_2(-h) \\ F_2(0) \end{bmatrix} = N_2(h) \begin{bmatrix} \sigma_2^{-1} F_1(-h) \\ \sigma_2^{-1} F_1(0) \end{bmatrix}, \quad (27)$$

where

$$M_2(h) = \begin{bmatrix} 1 + g_h(L_2) \partial_2 \sigma_2^{-1} \partial_1 & -f_h(L_2) \\ -f_h(L_2) \partial_2 \sigma_2^{-1} \partial_1 & L_2 g_h(L_2) + \partial_2 \sigma_2^{-1} \partial_1 \end{bmatrix},$$

$$N_2(h) = \begin{bmatrix} -g_h(L_2)(\partial_1^2 - L_2) & 0 \\ f_h(L_2)(\partial_1^2 - L_2) & -(\partial_1^2 - L_2) \end{bmatrix}. \quad (28)$$

At this stage, the combination of Eqs. (23) and (27) gives the general solution of Maxwell's equations in the superlayer made of the two layers. These equations can be considered as four relationships between six elements of \mathcal{H}_1 since, from Eq. (2), this Hilbert space is isomorph to \mathcal{H}_2 . In the general case of an superlayer made of m layers, one obtains $2m$ relationships between $2m+2$ elements of \mathcal{H}_1 . So, in order to obtain two additional relationships, the next step consists of imposing the condition at the boundaries of the “superlayer,” i.e., at planes defined by equations $x_3 = h$ and $x_3 = -h$. Herein, we impose the periodic boundaries condition in order to obtain Bloch solution in the crystal.

Let $\mathbf{d}_3 = d_{3,1} \mathbf{e}_1 + d_{3,2} \mathbf{e}_2 + d_{3,3} \mathbf{e}_3$ be the third spatial period of the woodpile crystal. Then, in addition to Eq. (3), we have

$$\nu(\mathbf{x} + \mathbf{d}_3) = \nu(\mathbf{x}), \quad \mathbf{x} \in \mathbb{R}^3, \quad (29)$$

where $\nu = \varepsilon, \mu$, and $d_{3,3} = 2h$ since the crystal is generated by the superlayer of thickness $2h$. Now, we define the translation operator T acting on \mathcal{H}_1 by

$$(T\psi)(x_1, x_2) = \psi(x_1 + d_{3,1}, x_2 + d_{3,2}) \quad (x_1, x_2) \in V. \quad (30)$$

So, finally, a Bloch solution in the woodpile crystal has to satisfy Eqs. (23), (27), and

$$\begin{bmatrix} TF_1(h) \\ TF_2(h) \end{bmatrix} = \exp(2i\pi k_3) \begin{bmatrix} F_1(-h) \\ F_2(-h) \end{bmatrix}, \quad (31)$$

where k_3 is fixed in $[-1/2, 1/2]$.

C. The numerical method

In this section, we give an explicit expression for the R matrix associated with a stack of layers that can be used directly in numerical computations. This R matrix gives the general solution of the homogeneous Eq. (1).

1. The expression of the R matrix for a single layer

We consider the same layer as in Secs. III B 1, III B 2, and III B 3. Appendix A shows how to determine in a general case the eigenvalues $\{\lambda_n | n \in \mathbb{N}\}$ of the operator L_1 , the associated eigenfunctions $\{\phi_n | n \in \mathbb{N}\}$ and the set of functions $\{\psi_n | n \in \mathbb{N}\}$ defined by

$$\psi_n = \sigma_1^{-1} \partial_1 \sigma_1 \phi_n, \quad L_1 \phi_n = \lambda_n \phi_n, \quad n \in \mathbb{N}. \quad (32)$$

We denote by $\langle \cdot, \cdot \rangle_{\mathcal{H}_1}$ the inner product in \mathcal{H}_1 . Since L_1 is self-adjoint in \mathcal{H}_1 , we can normalize its eigenfunctions such that they form an orthonormal set

$$\langle \phi_n, \phi_n \rangle_{\mathcal{H}_1} = 1, \quad \langle \phi_m, \phi_n \rangle_{\mathcal{H}_1} = 0, \quad m \neq n. \quad (33)$$

The eigenfunctions of the operator L_1 are also eigenfunctions of the operators ∂_2 and ∂_2^2 (Appendix A). Let $\{ik_{2,n} | n \in \mathbb{N}\}$ and $\{-k_{2,n}^2 | n \in \mathbb{N}\}$ be the associated sets of eigenvalues:

$$\partial_2 \phi_n = ik_{2,n} \phi_n, \quad \partial_2^2 \phi_n = -k_{2,n}^2 \phi_n, \quad n \in \mathbb{N}. \quad (34)$$

For the sake of clarity, the operators $M_1(h)$ and $N_1(h)$ are expressed in block forms.

$$M_1(h) = \begin{bmatrix} M_{1,11} & 0 \\ M_{1,21} & M_{1,22} \end{bmatrix}, \quad N_1(h) = \begin{bmatrix} N_{1,11} & N_{1,12} \\ N_{1,21} & N_{1,22} \end{bmatrix}. \quad (35)$$

Then, the expression of operators $M_1(h)$ and $N_1(h)$ developed on the eigenfunctions of L_1 can be deduced from the coefficients

$$\begin{aligned} \langle \phi_m, M_{1,11} \phi_n \rangle_{\mathcal{H}_1} &= \langle \phi_m, \phi_n \rangle_{\mathcal{H}_1} \\ &\quad - g_h(\lambda_m) ik_{2,n} \langle \psi_m, \sigma_1^{-1} \phi_n \rangle_{\mathcal{H}_1}, \\ \langle \phi_m, M_{1,12} \phi_n \rangle_{\mathcal{H}_1} &= f_h(\lambda_m) \langle \phi_m, \phi_n \rangle_{\mathcal{H}_1}, \\ \langle \phi_m, M_{1,21} \phi_n \rangle_{\mathcal{H}_1} &= f_h(\lambda_m) ik_{2,n} \langle \psi_m, \sigma_1^{-1} \phi_n \rangle_{\mathcal{H}_1}, \\ \langle \phi_m, M_{1,22} \phi_n \rangle_{\mathcal{H}_1} &= \lambda_m g_h(\lambda_m) \langle \phi_m, \phi_n \rangle_{\mathcal{H}_1} \\ &\quad - ik_{2,n} \langle \psi_m, \sigma_1^{-1} \phi_n \rangle_{\mathcal{H}_1}, \\ \langle \phi_m, N_{1,11} \phi_n \rangle_{\mathcal{H}_1} &= -g_h(\lambda_m) (\lambda_m + k_{2,m}^2) \langle \phi_m, \phi_n \rangle_{\mathcal{H}_1}, \\ \langle \phi_m, N_{1,21} \phi_n \rangle_{\mathcal{H}_1} &= f_h(\lambda_m) (\lambda_m + k_{2,m}^2) \langle \phi_m, \phi_n \rangle_{\mathcal{H}_1}, \end{aligned}$$

$$\langle \phi_m, N_{1,22} \phi_n \rangle_{\mathcal{H}_1} = -(\lambda_m + k_{2,m}^2) \langle \phi_m, \phi_n \rangle_{\mathcal{H}_1}, \quad (36)$$

where m, n are in \mathbb{N} , and where we used the identities $\langle \phi_m, [\partial_1 \sigma_1^{-1}] \phi_n \rangle_{\mathcal{H}_1} = \langle \psi_m, \sigma_1^{-1} \phi_n \rangle_{\mathcal{H}_1}$, $f_h(L_1) \phi_m = f_h(\lambda_m) \phi_m$, and $g_h(L_1) \phi_m = g_h(\lambda_m) \phi_m$.

Numerically, the operators $M_2(h)$ and $N_2(h)$ are truncated in order to get matrices. Hence, we have to choose a finite set of eigenvalues and eigenfunctions. From Eq. (14), each eigenvalue of L_1 is either an eigenvalue of L_{ε_1} or an eigenvalue of L_{μ_1} : we denote the set of eigenvalues of these scalar operators by $\{\lambda_{\varepsilon_1, p} | p \in \mathbb{N}\}$ and $\{\lambda_{\mu_1, p} | p \in \mathbb{N}\}$, respectively, and we number them such that

$$\omega^2 \varepsilon_+ \mu_+ \geq \lambda_{\nu_1, 1} \geq \lambda_{\nu_1, 2} \cdots \geq \lambda_{\nu_1, p} \cdots, \quad (37)$$

where $\nu_1 = \varepsilon_1, \mu_1$. Then, the considered set of eigenvalues is

$$\Lambda_{1, \mathcal{N}} = \{\lambda_{\nu_1, p} | p \leq \mathcal{N}, \nu_1 = \varepsilon_1, \mu_1\}, \quad (38)$$

where \mathcal{N} is an integer. For all $n = 1, 2, \dots, 2\mathcal{N}$, the eigenvalue λ_n can be defined by $\lambda_n = \lambda_{\varepsilon_1, p}$ if $n = 2p - 1$ and $\lambda_n = \lambda_{\mu_1, p}$ if $n = 2p$, where $p = 1, 2, \dots, \mathcal{N}$. Let $\tilde{K}_{\mathcal{N}}$ be the matrix associated with the operator K with coefficients $\langle \phi_m, K \phi_n \rangle_{\mathcal{H}_1}$. The choice of the set of eigenvalues (38) is justified since, for example, the difference between the operator $[f_h(L_1) - 1]$ and the associated matrix $[f_h(\tilde{L}_{1, \mathcal{N}}) - \tilde{I}_{\mathcal{N}}]$ is less than $2 \max\{\exp(-\sqrt{|\lambda_{\varepsilon_1, \mathcal{N}}|} h), \exp(-\sqrt{|\lambda_{\mu_1, \mathcal{N}}|} h)\}$ if $\lambda_{\varepsilon_1, \mathcal{N}}$ and $\lambda_{\mu_1, \mathcal{N}}$ are negative; the convergence is exponential for this compact operator.

Now, from coefficients (36), we obtain the expression of the R matrix associated with the considered layer

$$\tilde{R}_{1, \mathcal{N}} = \begin{bmatrix} \tilde{N}_{1,11, \mathcal{N}} & 0 \\ \tilde{N}_{1,21, \mathcal{N}} & \tilde{N}_{1,22, \mathcal{N}} \end{bmatrix}^{-1} \begin{bmatrix} \tilde{M}_{1,11, \mathcal{N}} & \tilde{M}_{1,12, \mathcal{N}} \\ \tilde{M}_{1,21, \mathcal{N}} & \tilde{M}_{1,22, \mathcal{N}} \end{bmatrix}. \quad (39)$$

Note that this R matrix is expressed using the set of eigenfunctions of L_1 and the inner product $\langle \cdot, \cdot \rangle_{\mathcal{H}_1}$ in \mathcal{H}_1 . Moreover, from Eqs. (23), (35), and (39), this matrix $\tilde{R}_{1, \mathcal{N}}$ connects the values of F_1 and $\sigma_1^{-1} F_2$ at the planes delimiting the layer. Thus, expression (39) for the R matrix cannot be used to connect the solution of the considered layer to the solutions of the adjacent layers. An expression in a basis, independent of the layer, is then necessary.

Let \mathcal{H} be an Hilbert space isomorph to \mathcal{H}_1 and $\langle \cdot, \cdot \rangle_{\mathcal{H}}$ the inner product in this new Hilbert space. In practice, \mathcal{H} can be $L_{k_1, k_2}^2(V, dx_1 dx_2; \mathbb{C}^2)$, i.e., the set of locally square integrable and \mathbb{C}^2 -valued functions with the boundary condition (8) and the usual inner product. Let $\{e_n | n \in \mathbb{N}\}$ be an orthonormal basis of \mathcal{H} (in practice, this set can be the plane waves basis since it will not lead to convergence problems in woodpile structures). The expression of the R matrix in this new basis is

$$R_{1, \mathcal{N}} = \begin{bmatrix} Q_{\mathcal{N}}^{-1} & 0 \\ 0 & Q_{\mathcal{N}}^{-1} \end{bmatrix} \tilde{R}_{1, \mathcal{N}} \begin{bmatrix} P_{\mathcal{N}} & 0 \\ 0 & P_{\mathcal{N}} \end{bmatrix}, \quad (40)$$

where $P_{\mathcal{N}}$ and $Q_{\mathcal{N}}$ are, respectively, the matrices with coefficients $\langle e_m, \phi_n \rangle_{\mathcal{H}}$ and $\langle e_m, \sigma_1 \phi_n \rangle_{\mathcal{H}}$, $m, n = 1, 2, \dots, 2\mathcal{N}$. We denote by $\psi_{\mathcal{N}}$ the column vector associated with the vector ψ in \mathcal{H} with coefficients $\langle e_n, \psi \rangle_{\mathcal{H}}$, $n = 1, 2, \dots, 2\mathcal{N}$. Then, from Eqs. (23), (35), (39), and (40), we obtain the relationship

$$\begin{bmatrix} F_{2,\mathcal{N}}(0) \\ F_{2,\mathcal{N}}(h) \end{bmatrix} = R_{1,\mathcal{N}} \begin{bmatrix} F_{1,\mathcal{N}}(0) \\ F_{1,\mathcal{N}}(h) \end{bmatrix}, \quad (41)$$

which gives the general numerical solution of Maxwell's equations in the layer.

2. The expression of the R matrix for a stack of layers

We consider here the same superlayer as in Sec. III B 4. From the operators $M_2(h)$ and $N_2(h)$ (28), we obtain the R matrix $R_{2,\mathcal{N}}$ associated with the bottom layer. This R matrix gives the relationship

$$\begin{bmatrix} F_{2,\mathcal{N}}(-h) \\ F_{2,\mathcal{N}}(0) \end{bmatrix} = R_{2,\mathcal{N}} \begin{bmatrix} F_{1,\mathcal{N}}(-h) \\ F_{1,\mathcal{N}}(0) \end{bmatrix}. \quad (42)$$

$$R_{1,\mathcal{N}} \star R_{2,\mathcal{N}} = \begin{bmatrix} R_{2,11,\mathcal{N}} - R_{2,12,\mathcal{N}}(R_{2,22,\mathcal{N}} - R_{1,11,\mathcal{N}})^{-1} R_{2,21,\mathcal{N}} & R_{2,12,\mathcal{N}}(R_{2,22,\mathcal{N}} - R_{1,11,\mathcal{N}})^{-1} R_{1,12,\mathcal{N}} \\ -R_{1,21,\mathcal{N}}(R_{2,22,\mathcal{N}} - R_{1,11,\mathcal{N}})^{-1} R_{2,21,\mathcal{N}} & R_{1,22,\mathcal{N}} - R_{1,21,\mathcal{N}}(R_{2,22,\mathcal{N}} - R_{1,11,\mathcal{N}})^{-1} R_{1,12,\mathcal{N}} \end{bmatrix}. \quad (45)$$

Note that the group law \star associated with this R -matrix algorithm is exactly the same as the one defined in Ref. [39]. This continuation algorithm will not lead to numerical instabilities since it is derived from the continuation procedure defined in Sec. III B 2. In the general case of an superlayer made of m layers, one just has to combine m R matrices using the law \star [39].

Finally, we show how to use the translation T (30) in order to obtain the R matrix associated with the superlayer that generates the woodpile crystal considered in Sec. III B 4. The translation T can be considered as the basis change from $\{e_n | n \in \mathbb{N}\}$ to $\{T^{-1}e_n | n \in \mathbb{N}\}$ since, from the unitarity $T^{-1} = T^*$, $\langle e_n, T\psi \rangle_{\mathcal{H}} = \langle T^{-1}e_n, \psi \rangle_{\mathcal{H}}$, where ψ is in \mathcal{H} and n is an integer. Hence, the final R matrix is

$$R_{\mathcal{N}} = \begin{bmatrix} 1_{\mathcal{N}} & 0 \\ 0 & T_{\mathcal{N}} \end{bmatrix} R_{1,\mathcal{N}} \star R_{2,\mathcal{N}} \begin{bmatrix} 1_{\mathcal{N}} & 0 \\ 0 & T_{\mathcal{N}}^{-1} \end{bmatrix}, \quad (46)$$

where $1_{\mathcal{N}}$ and $T_{\mathcal{N}}$ are, respectively, the matrices with coefficients $\langle e_m, e_n \rangle_{\mathcal{H}}$ and $\langle e_m, Te_n \rangle_{\mathcal{H}}$, $m, n = 1, 2, \dots, 2\mathcal{N}$. From Eq. (43), this matrix gives the relationship

$$\begin{bmatrix} F_{2,\mathcal{N}}(-h) \\ TF_{2,\mathcal{N}}(h) \end{bmatrix} = R_{\mathcal{N}} \begin{bmatrix} F_{1,\mathcal{N}}(-h) \\ TF_{1,\mathcal{N}}(h) \end{bmatrix}. \quad (47)$$

IV. VERIFICATION OF THE NUMERICAL METHOD

In this section, we check the numerical method we have presented. For this aim, we realize a convergence test, we

In this section, we will show how to combine the two matrices $R_{1,\mathcal{N}}$ and $R_{2,\mathcal{N}}$ to obtain the R matrix associated with the superlayer. This combination of the two R matrices (or the R -matrix algorithm [39]) can be considered as an associative group law denoted by the symbol \star [39].

Similarly to $R_{2,\mathcal{N}}$ (41) and $R_{1,\mathcal{N}}$ (42), the R matrix $R_{1,\mathcal{N}} \star R_{2,\mathcal{N}}$ associated with the stack of the two layers provides the following relationship:

$$\begin{bmatrix} F_{2,\mathcal{N}}(-h) \\ F_{2,\mathcal{N}}(h) \end{bmatrix} = R_{1,\mathcal{N}} \star R_{2,\mathcal{N}} \begin{bmatrix} F_{1,\mathcal{N}}(-h) \\ F_{1,\mathcal{N}}(h) \end{bmatrix}. \quad (43)$$

The comparison of Eqs. (41)–(43) shows that the expression for the matrix $R_{1,\mathcal{N}} \star R_{2,\mathcal{N}}$ can be deduced from Eqs. (41) and (42) by eliminating the vectors $F_{2,\mathcal{N}}(0)$ and $F_{1,\mathcal{N}}(0)$. Thus, the matrices $R_{1,\mathcal{N}}$ and $R_{2,\mathcal{N}}$ are expressed in block forms

$$R_{j,\mathcal{N}} = \begin{bmatrix} R_{j,11,\mathcal{N}} & R_{j,12,\mathcal{N}} \\ R_{j,21,\mathcal{N}} & R_{j,22,\mathcal{N}} \end{bmatrix}, \quad j=1,2. \quad (44)$$

Then, after the elimination of the vectors $F_{2,\mathcal{N}}(0)$ and $F_{1,\mathcal{N}}(0)$ in Eqs. (41) and (42), we obtain

check energy conservation and we compare the theoretical calculations to the experimental measurements. These three checks focus on the reflection properties of an experimentally realized woodpile structure [12] designed to present a band gap around the wavelength equal to $1.5 \mu\text{m}$.

The considered woodpile structure consists of a stack of five identical layers made of rectangular silicon rods (Fig. 4). The silicon rods have a height equal to $h = 200 \text{ nm}$ and width equal to $w = 180 \text{ nm}$ and their axis to axis spacing is $d_{1,1} = d_{2,2} = 650 \text{ nm}$. The layers are stacked such that two first neighbors are perpendicular and two second neighbors are displaced relative to each other by $d_{3,1} = d_{1,1}/2 = 325 \text{ nm}$ and $d_{3,2} = d_{2,2}/2 = 325 \text{ nm}$. The media above and below the structure are, respectively, air and silicon. Finally, there is a

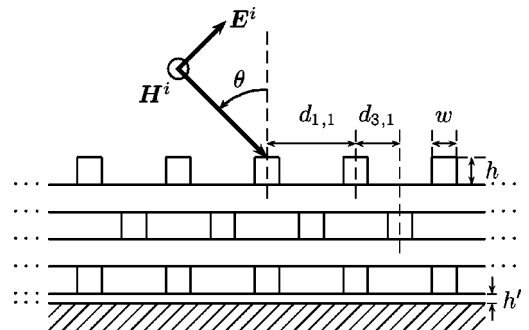


FIG. 4. Representation in the incidence plane of the considered woodpile structure: the parameters of the structure are given in the text; the incident electromagnetic field E^i, H^i is p polarized.

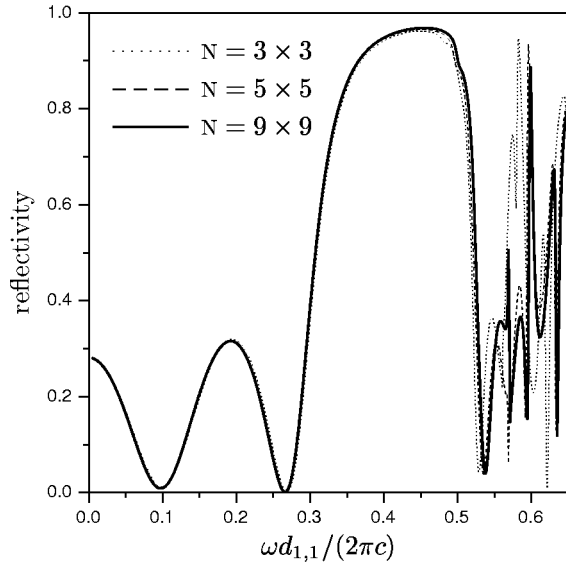


FIG. 5. Reflectivity as a function of the normalized frequency $\omega d_{1,1}/(2\pi c)$ with $d_{1,1}=0.65 \mu\text{m}$ showing the convergence when the integer \mathcal{N} is increasing; the considered structure and incident electromagnetic field are represented in Fig. 4.

thin silicon nitride layer with height equal to $h' = 70 \text{ nm}$ (optical index chosen equal to 2.0 [49]) between the structure and the silicon substrate. The optical index of silicon is chosen to be equal to 3.45 (corresponding to the value at a wavelength of $1.5 \mu\text{m}$ [49]).

The woodpile structure is illuminated from the air by a plane wave: its wave vector is perpendicular to the axis of the rods of the first layer and its direction differs from the vertical axis by the angle θ equal to 20° (Fig. 4). The incident plane wave is p polarized, i.e., the incident electric field \mathbf{E}^i is inside the incidence plane and the incident magnetic field \mathbf{H}^i is perpendicular to this plane.

A. Convergence test

Figure 5 shows the reflectivity as a function of the normalized frequency $\omega d_{1,1}/(2\pi c)$ for different values of the integer \mathcal{N} . We varied the normalized frequency from 0 to 0.65. This range corresponds to wavelengths ranging from $1 \mu\text{m}$ to ∞ if the spatial period $d_{1,1}$ is equal to $0.65 \mu\text{m}$ as for the experimental realization [12]. Note that it includes the important wavelengths around $1.5 \mu\text{m}$ [corresponding to $\omega d_{1,1}/(2\pi c) = 0.65/1.5 \sim 0.43$], where reflectivity is close to 100% for the considered incident plane wave. The given reflectivity curves are obtained with the three values 9×9 , 5×5 , and 3×3 of the integer \mathcal{N} .

If the integer \mathcal{N} is equal to 9×9 (solid line on Fig. 5), the obtained curve has completely converged since it is impossible to distinguish it from a curve obtained with a higher value of \mathcal{N} . If \mathcal{N} is equal to 5×5 (dashed line in Fig. 5), the obtained curve is very close to the converged one for all considered frequencies. This second number is sufficient to obtain appreciable precision while, for the considered structure, the CPU time for a one point computation is less than 1 s on a PC equipped with a 1 GHz Pentium III processor.

Finally, if \mathcal{N} is equal to 3×3 (dotted line in Fig. 5), the obtained curve differs significantly from the converged one only for the normalized frequencies up to the band gap. This last number is sufficient to obtain an estimate around the band gap (especially to obtain an estimate of the band gap edges), while the CPU time for a one point computation becomes less than 0.2 s.

This convergence test confirms the one done for the band gap edge and reported in Ref. [36] [Table 1]: for both reflectivity and dispersion relation, the value 5×5 for the integer \mathcal{N} is in practice sufficient. The associated CPU time is then close to the one needed for the two-dimensional crystals.

B. Test of energy conservation

Since there is no absorption in the considered structure (ε and μ are real-valued functions), we can check energy conservation by comparing the flux of the Poynting vector associated with the incident plane wave (normalized to unity) and the sum of the calculated flux of the Poynting vector associated with the reflected and transmitted fields (reflectivity and transmittance). The difference gives the energy conservation error due to the matrix truncation (indeed, this error is equal to zero if the matrices are not truncated).

This test is possible if the matrix truncation is such that energy conservation [37] is not automatically satisfied. In the numerical method we have presented, the energy conservation can be broken due to the basis change (40). The expressions for the matrices $P_{\mathcal{N}}$ and $Q_{\mathcal{N}}$ given in Sec. III C 1 are such that the energy conservation is actually broken. In order to save matrix inversion and then computation time, one could be tempted to use the fact that the adjoint of the non-truncated matrix with coefficients $\langle e_m, \phi_n \rangle_{\mathcal{H}}$ is exactly the inverse of the nontruncated matrix with coefficients $\langle \phi_m, e_n \rangle_{\mathcal{H}_1}$; the adjoint of the matrix $P_{\mathcal{N}}$ is related to the inverse of the matrix $Q_{\mathcal{N}}$. We do not recommend to use this property for reflectivity computations since it will provide a R matrix which implies the energy conservation rigorously.

The link between energy conservation and the truncation procedure can be stated clearly. The vertical component of the Poynting vector is the real part of $[E_1 \bar{H}_2 - E_2 \bar{H}_1]/2$ and, with notation (12), its flux through the plane defined by the equation $x_3 = \pm h$ can be written as

$$\text{Re}[\langle F_2(\pm h), JF_1(\pm h) \rangle_{\mathcal{H}}]/2, \quad J = \begin{bmatrix} 0 & -1 \\ 1 & 0 \end{bmatrix}.$$

Then, from Eq. (47), the flux of the Poynting vector through the planes with equations $x_3 = \pm h$ are rigorously equal if and only if the matrix $R_{\mathcal{N}}$ is related to its adjoint $R_{\mathcal{N}}^*$ by

$$R_{\mathcal{N}}^* = - \begin{bmatrix} J_{\mathcal{N}} & 0 \\ 0 & -J_{\mathcal{N}} \end{bmatrix} R_{\mathcal{N}} \begin{bmatrix} J_{\mathcal{N}} & 0 \\ 0 & -J_{\mathcal{N}} \end{bmatrix}, \quad (48)$$

where $J_{\mathcal{N}}$ is the matrix with coefficients $\langle e_m, J e_n \rangle_{\mathcal{H}}$, $m, n = 1, 2, \dots, 2\mathcal{N}$. Relation (48), which is equivalent to the energy conservation together with the reciprocity theorem [37], is satisfied if one uses the adjoint of matrix $P_{\mathcal{N}}$ to express the

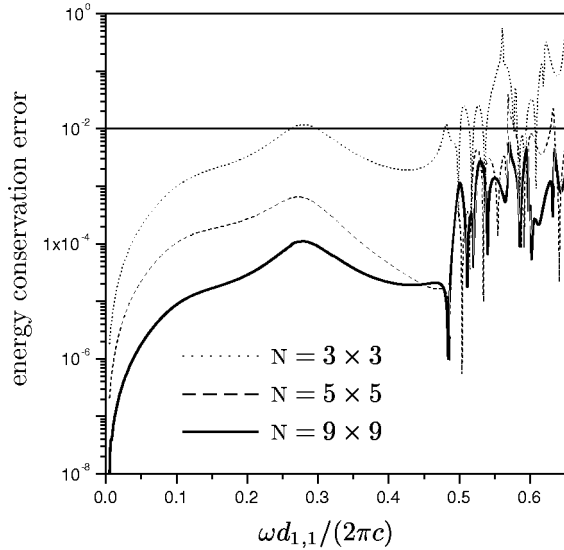


FIG. 6. Error on energy conservation as a function of the normalized frequency corresponding to Fig. 5; the considered structure and incident electromagnetic field are represented in Fig. 4.

matrix Q_N^{-1} in Eq. (40). The truncation procedure and its consequences on the reciprocity theorem is also discussed in Refs. [26,50].

Figure 6 shows the energy conservation error as a function of the normalized frequency $\omega d_{1,1}/(2\pi c)$ for the three values 9×9 , 5×5 , and 3×3 of the integer N corresponding to Fig. 5. This test on energy conservation confirms the preceding test of convergence. If N is equal to 9×9 (solid line), the error is always smaller than 0.5%. If N is equal to 5×5 (dashed line), the error is rarely above 1% and always under 5%; this precision is acceptable in practice. Finally, if N is equal to 3×3 (dotted line), the error is less than 1.5% and acceptable for the normalized frequencies around the band gap.

C. Experimental verification

In this section, we compare our numerical results with measured reflectivity data. This comparison completes the study presented in Ref. [27]. There we showed that it is necessary to take into account the following structural perturbation: in each layer, every two rods are slightly shifted (Fig. 7). So, in this section, the considered structure has horizontal spatial periods $d_{1,1} = d_{2,2} = 1300$ nm. From the image presented in Ref. [27], we have chosen a shift δ of 50 nm and then, in each layer, the axis to axis spacing of two consecutive rods is alternatively $d'_{1,1} = 700$ nm and $d''_{1,1} = 600$ nm (Fig. 7). This slight shift is the only difference between the structure considered in this section and the structure considered previously and represented in Fig. 4. From now, we denote by “ideal” the woodpile without structural perturbation represented in Fig. 4.

In Ref. [27], the comparisons between calculated and measured reflectivity with different angles θ , structure orientations and polarizations are presented. In this paper, we focus on the single case represented in Figs. 4 and 7 with the

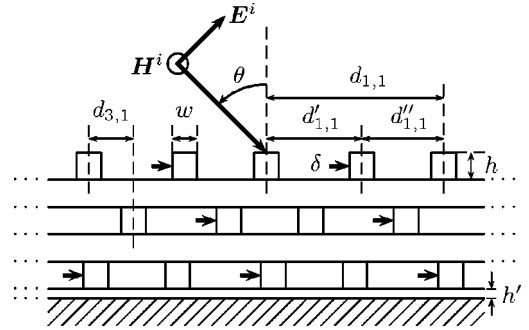


FIG. 7. Representation in the incidence plane of the considered woodpile structure for the experimental validation; the single difference between this structure and the ideal one represented in Fig. 4 is that, in each layer, every second rods is shifted with $\delta = 50$ nm.

angle θ equal to 20° . However, in order to complete the study presented in Ref. [27], we take into account the wavelength dependence of the silicon (the values of the optical index for the silicon are taken from Ref. [49]).

Note that, contrary to the ideal woodpile of previous sections, the woodpile with the structural perturbation (Fig. 7) is not invariant under reflections with respect to vertical planes containing the incident electric field E^i and magnetic field H^i . Consequently, the electric field (and then the reflected electric field) is not contained in the incoming plane and, the magnetic field (and then reflected magnetic field) is not perpendicular to the incoming plane. Moreover, since the spatial period of the woodpile with the structural perturbation is quite large, there are several reflected orders. Since the experimental measurements provide the reflectivity associated with the p -polarized field component in the specular order, we have to consider only this component of the reflected field.

Figure 8 shows the experimental measurements (represented by the open circles) of the reflectivity associated with the p -polarized field component in the specular order. The details about these experimental measurements are presented in Ref. [27]. Figure 8 shows also the calculated reflectivity (represented by the solid line) on the woodpile with the structural perturbation of Fig. 7. The integer N was chosen equal to 10×11 for this calculation leading to an error less than 5% for the wavelengths ranging from $1 \mu\text{m}$ to $1.2 \mu\text{m}$ and less than 2% for the other wavelengths (note that we have neglected the imaginary part of the optical index of the silicon for this test on energy conservation). Moreover, we have realized a convergence test showing that the calculations of Fig. 8 have converged.

The comparison of the experimental measurements and calculations shows an excellent agreement for the wavelengths ranging from $1.25 \mu\text{m}$ to $1.7 \mu\text{m}$. In particular, the position and the width of the dip around $1.42 \mu\text{m}$ are very well reproduced by the calculations, the difference of depth being certainly the result of the averaging of the experimental setup.

The comparison for the wavelengths ranging from $1 \mu\text{m}$ to $1.25 \mu\text{m}$ shows a significant difference. That is why we have also represented by a dashed line on Fig. 8 the calcu-

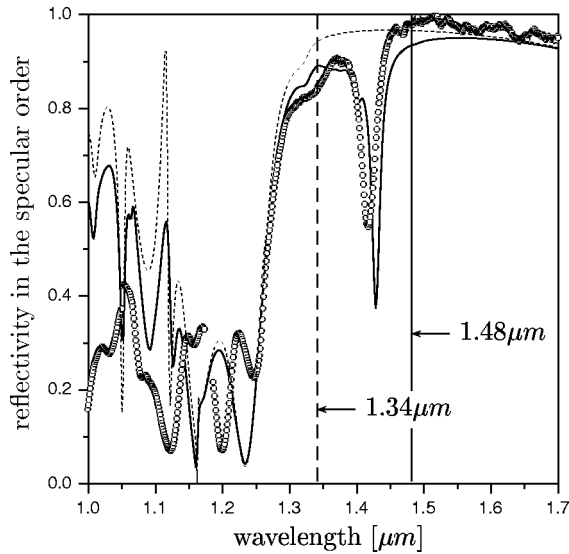


FIG. 8. Reflectivity associated with the p -polarized field component in the specular order as a function of the wavelength (the length unity is the micrometer): the open circles (\circ) correspond to the experimental measurements; the solid line corresponds to the calculated reflectivity on the woodpile with the structural perturbation (Fig. 7); the dashed line corresponds to the calculated reflectivity on the ideal woodpile (Fig. 4). The solid vertical line at $1.48 \mu\text{m}$ corresponds to the calculated band gap edge in the woodpile with the structural perturbation; the dashed vertical line at $1.34 \mu\text{m}$ corresponds to the calculated band gap edge in the ideal woodpile.

lated reflectivity on the ideal woodpile and taking into account the wavelength dependence of the silicon. The differences between the two calculated curves only come from the slight shift. The comparison of the two calculated curves shows that a small structural perturbation can lead to a non-negligible difference for the wavelengths ranging from $1 \mu\text{m}$ to $1.25 \mu\text{m}$. So, we conclude that the significant difference between the experimental measurements and calculations is likely to be the result of many slight structural perturbations in the experimental realization, which have not been taken into account in the calculations.

Finally, as mentioned in Ref. [27], the difference between the two calculated curves for the wavelengths ranging from $1.25 \mu\text{m}$ to $1.7 \mu\text{m}$ is the result of the “superstructure:” the horizontal spatial periods of the woodpile with the structural perturbation are twice as large as that of the ideal structure. Figure 9 shows the representation of the dispersion relation in the ideal structure (the details about this representation are presented in Ref. [36]). Note that, in this paper, the frequency dependence of the optical index of silicon is taken into account for the dispersion relation. The imaginary part of the optical index is neglected for this dispersion relation (although it is not for the reflectivity curves in Fig. 8), but this does not make problem since this imaginary part is always smaller than 0.006. From Fig. 9, a photonic band gap exists for normalized frequencies ranging from $\omega_- d_{1,1}/(2\pi c) \approx 0.356$ to $\omega_+ d_{1,1}/(2\pi c) \approx 0.434$. The wavelengths corresponding to these lower (ω_-) and upper (ω_+) band gap edges are, respectively, $1.83 \mu\text{m}$ and $1.50 \mu\text{m}$.

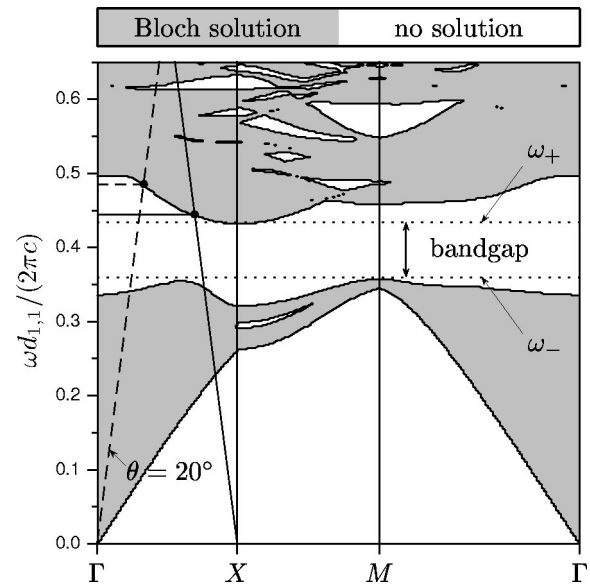


FIG. 9. Representation of the dispersion relation in the ideal woodpile structure represented in Fig. 4: in abscissa, the tangential component (k_1, k_2) of the Bloch wave vector on the characteristic path $\Gamma X M \Gamma$, where Γ , X , and M have, respectively, the coordinates $(0,0)$, $(0,0.5)$, and $(0.5,0.5)$; in ordinate, the normalized frequency with $d_{1,1} = 0.65 \mu\text{m}$; the frequency dependence of the optical index of silicon is taken into account (the imaginary part of this optical index is neglected). The horizontal dotted lines correspond to the band gap edges: the frequency ω_+ corresponding to the upper band gap edge is at $\omega d_{1,1}/(2\pi c) \approx 0.434$ and the frequency ω_- corresponding to the lower band gap edge is at $\omega d_{1,1}/(2\pi c) \approx 0.356$. The dashed line starting from Γ corresponds to the curves in Figs. 5 and 8 when the angle θ is equal to 20° : it defines the upper band gap edge (horizontal dashed line) for $\theta = 20^\circ$ at $\omega d_{1,1}/(2\pi c) \approx 0.484$; the horizontal solid line is at $\omega d_{1,1}/(2\pi c) \approx 0.443$.

The dashed line starting from Γ is defined by the equation $[\omega d_{1,1}/(2\pi c)] \sin \theta = k_1$, where θ is equal to 20° and it then corresponds to the reflectivity curves of Fig. 8. So, from Fig. 9, the upper band gap edge for this external angle θ is at $\omega d_{1,1}/(2\pi c) \approx 0.484$ corresponding to the wavelength $1.34 \mu\text{m}$. We have represented this upper band gap edge in Fig. 8 by the vertical dashed line. One may remark that the dip is then included inside the band gap of the ideal structure. Now, let us consider the woodpile with the structural perturbation. Since the horizontal spatial periods are twice as large as that of the ideal structure, the dispersion relation in this structure can be roughly obtained by folding the dispersion relation in the ideal structure as it is shown in Ref. [27]. So, the solid line starting from X in Fig. 9 provides an estimate of the upper band gap edge in the woodpile with the structural perturbation at $\omega d_{1,1}/(2\pi c) \approx 0.443$ corresponding to a wavelength of $1.47 \mu\text{m}$. A rigorous calculation that takes into account the structural perturbation gives this upper band gap edge at $1.48 \mu\text{m}$. We have represented this upper band gap edge in Fig. 8 by the vertical solid line. Then the presence of the dip around $1.42 \mu\text{m}$ is not surprising since this wavelength is not inside the band gap of the woodpile with the structural perturbation. Finally, for wavelengths ranging from $1.25 \mu\text{m}$ to $1.7 \mu\text{m}$, we can conclude that the

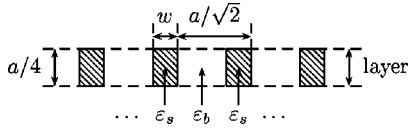


FIG. 10. Representation of the considered layer; the horizontal spatial periods are $d_{1,1}=d_{2,2}=a/\sqrt{2}$ and the height is $h=a/4$. The first dielectric rod of the unit cell of this layer has width w and dielectric constant ε_s and the second has dielectric constant ε_b .

presence of the dip is certainly the result of the the effect of the “superstructure.” Moreover, since the agreement between the calculations and the measurement is very good, we can also conclude that the periodic arrangement dominates over the other structural perturbations in this wavelength range.

V. PHOTONIC BAND GAPS IN WOODPILE STRUCTURES

In this section, we investigate the existence of photonic band gaps in woodpile structures. We consider a simple woodpile structure similar to the ones experimentally realized [12,13]. It is generated by the superlayer considered in Sec. III B 4 and represented in Fig. 3. The spatial periods d_1 , d_2 , and d_3 are chosen such that they generate a face-centered-cubic lattice in order to support the presence of photonic band gaps [3]. Let a be the edge length of the associated cube: $d_{1,1}=d_{2,2}=a/\sqrt{2}$, $d_{3,3}=a/2$, and $d_{3,1}=d_{3,2}=a/(2\sqrt{2})$. Since the considered superlayer is made of two layers that are identical after a rotation of 90° of one of them (Fig. 3), the height of these layers is $h=d_{3,3}/2=a/4$. Finally, each layer is made of two dielectric rods per unit cell as represented in Fig. 10. The relevant parameters are then the index contrast

$$\eta = \sqrt{\varepsilon_s/\varepsilon_b}, \quad (49)$$

and the filling ratio

$$f = w/d_{1,1} = \sqrt{2}w/a. \quad (50)$$

The quantity that we investigate is the relative band gap width

$$g = 2 \frac{\omega_+ - \omega_-}{\omega_+ + \omega_-}, \quad (51)$$

where ω_+ and ω_- are, respectively, the upper and the lower band gap edges as defined in Fig. 9. Note that, due to definition (51), g can be negative and the presence of a band gap is equivalent to $g > 0$.

The relative band gap width g depends on both index contrast η and filling ratio f . While it is well known that a high index contrast is more favorable to open a band gap, the influence of the filling ratio is not obvious. Indeed, contrary to the case of face-centered-cubic lattices of spheres [15], the band gap width g is not a monotone function of the filling ratio f [there is no band gap when f has its minimal (0) or maximal (1) values].

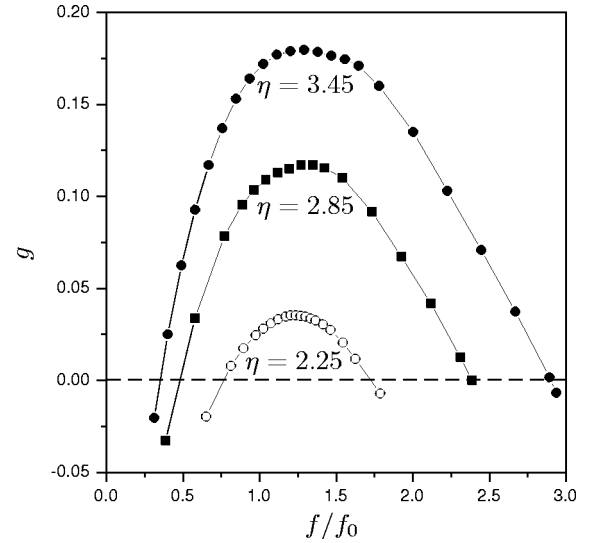


FIG. 11. Relative band gap width g as a function of the normalized filling ratio f/f_0 for different values of the index contrast η : the solid circles correspond to $\eta=3.45$, the solid squares correspond to $\eta=2.85$, and the open circles correspond to $\eta=2.25$.

So, in this section, we first determine the optimal filling ratio. Then, we determine minimal index contrast leading to a photonic band gap. Finally, we study the influence of structural perturbation similar to the one observed in the experimental realization.

A. Determination of the optimal filling ratio

Since the permittivity is a single variable function in each layer, we assume that the filling ratio

$$f_0 = (1 + \eta)^{-1}, \quad (52)$$

associated with the Bragg condition in one-dimensional systems, should play a vital role. This physical assumption is also supported by the fact that, in the mathematical formulation of Sec. III B, the operators L_1 (14) and L_2 (26) play a determinant role.

Figure 11 shows the relative band gap width (51) as a function of the filling ratio (50) for the three values 3.45, 2.85, and 2.25 of the index contrast (49). Note that convergence tests have been realized in order to ensure the accuracy of the results and to obtain an convenient precision as reported in Ref. [36]. The value 3.45 of the index contrast corresponds to the woodpile structure, we have studied in the preceding section: with the optimal value of the filling ratio at 0.29 ± 0.02 , the relative band gap width is equal to $17.9\% \pm 0.1\%$. Note that this result confirms the previous one presented in Ref. [19] so that, the filling ratio of the experimental realization [12,13] is certainly optimal. The value 2.25 of the index contrast can correspond to ordinary transparent materials in the optical range such as air and Ta_2O_5 [51]: with the optimal value of the filling ratio at 0.38 ± 0.02 , the relative band gap width is equal to $3.5\% \pm 0.1\%$.

For both values 3.45 and 2.25 of the index contrast, the filling ratio $f = 1.3f_0$ is very close to the optimal value. This is also confirmed for the values 2.85 (Fig. 11), 2.33, and 3.6

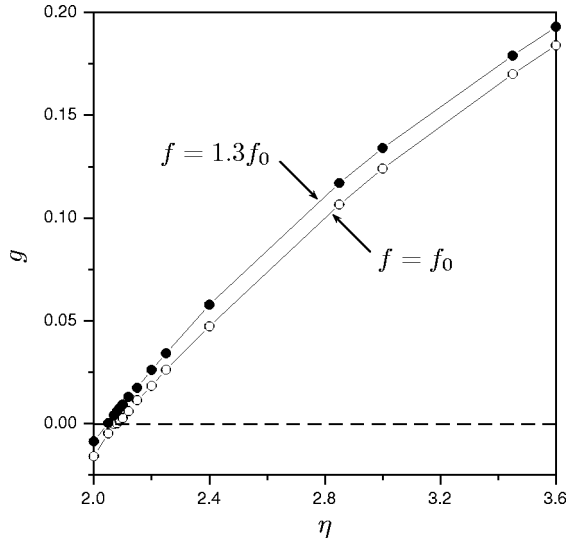


FIG. 12. Relative band gap width g as a function of the index contrast η : the solid circles correspond to the filling ratio $f = 1.3f_0$ and the open circles correspond to the filling ratio $f = f_0$.

[19]. Then, from these numerical studies, we conclude that the optimal value of the filling ratio is certainly around $f = 1.3f_0$ for the woodpile structure considered in this section.

B. Minimal index contrast needed for a photonic band gap

With this knowledge, we can vary the index contrast to search for the lowest possible value that opens a band gap. Figure 12 shows the relative band gap width as a function of the index contrast: with the filling ratio equal to $1.3f_0$ (solid circles), a band gap opens from an index contrast $\eta = 2.05 \pm 0.01$; with the filling ratio equal to f_0 (open circles), a band gap opens from an index contrast equal to $\eta = 2.08 \pm 0.01$. Note that the relative band gap width at $f = 1.3f_0$ is always larger than the one at $f = f_0$. This confirms the conclusion of the Sec. V A, so that the minimal index contrast leading to a photonic band gap is certainly around $\eta = 2.05 \pm 0.01$ associated with a filling ratio $f = 0.43 \pm 0.01$.

C. Woodpiles with contrast 2.25

In this section, we study the possibility for the realization of a photonic woodpile crystal with a photonic band gap in the optical and infrared ranges. We consider an index contrast $\eta = 2.25$ corresponding to that of air and tantalum pentoxide (Ta_2O_5) in these ranges. Note that this transparent dielectric material is used to realize planar multielectric structures at optical scale and to implant erbium ions [51]. From the study of Sec. V A, the relative band gap width is equal to $3.5\% \pm 0.1\%$ at the optimal value of the filling ratio at 0.38 ± 0.02 . However, this band gap exists in the ideal structure. So, we have to study the influence of the structural perturbations which appear in the experimental realizations.

The influence of many structural perturbations on the band gap in woodpile structures have been studied in Ref. [20]. However, this study does not contain the structural perturbation due to the fabrication techniques of the silicon

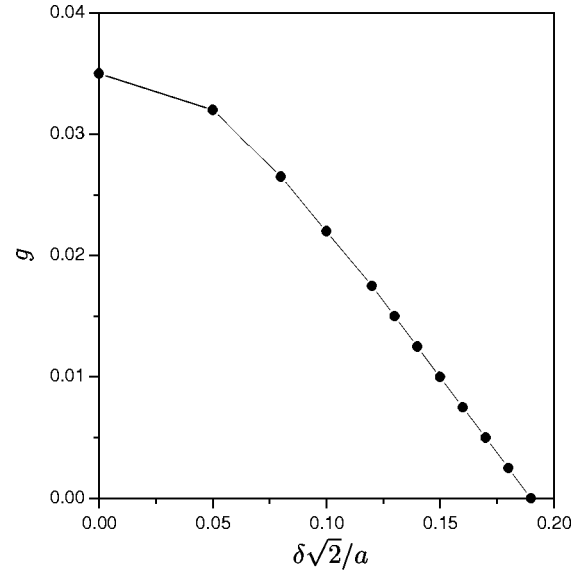


FIG. 13. Relative band gap width g as a function of the the normalized shift $\delta\sqrt{2}/a$.

woodpile crystal [12] considered in Sec. IV C and Ref. [27]. So, in order to complete the study presented in Ref. [20], we give in this section the influence of the shift δ for every two rods in the woodpile structure (Fig. 7).

Figure 13 shows the relative band gap width as a function of the shift δ . Note that the coefficient $a/\sqrt{2}$ for the normalization of the shift is equal to $d_{1,1} = d_{2,2}$ in the ideal structure and to $d_{1,1}/2 = d_{2,2}/2$ in the structure with the structural perturbation. From Fig. 13, the band gap opens for a shift δ ranging from 0.0 until $0.18a/\sqrt{2}$. In particular, for a shift equal to $0.10a/\sqrt{2}$, the relative band gap width is equal to $2.2\% \pm 0.1\%$.

Figure 14 shows a representation of the dispersion relation in the ideal woodpile structure (left) and in the structure

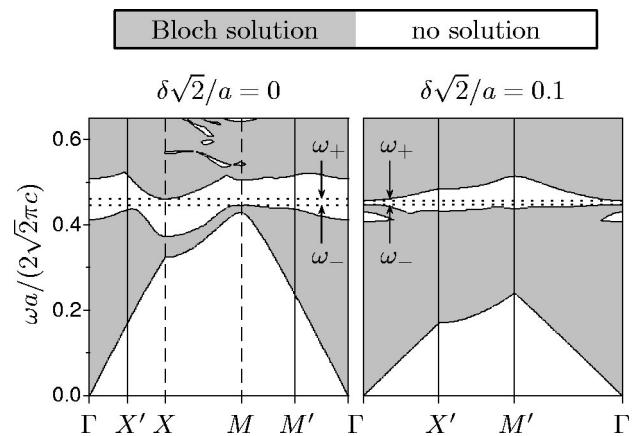


FIG. 14. Representation of the dispersion relation in the ideal woodpile structure (left) and in the structure with the structural perturbation at $\delta\sqrt{2}/a = 0.1$ (right): the index contrast η is equal to 2.25; the filling ratio f is equal to 0.38. The coordinates of Γ , X and M are reported in Fig. 9; in the same coordinates system associated with the dual lattice of the ideal structure, the coordinates of X' and M' are, respectively, $(0,0.25)$ and $(0.25,0.25)$.

with the structural perturbation at $\delta\sqrt{2}/a=0.1$ (right). These representations are similar to the one of Fig. 9. This figure shows that a band gap exists in both considered structures: the band gap edges in the ideal structure are at $\omega_+a/(2\sqrt{2}\pi c)=0.460\pm 0.001$ and $\omega_-a/(2\sqrt{2}\pi c)=0.445\pm 0.001$; the band gap edges in the structure with the structural perturbation ($\delta\sqrt{2}/a=0.1$) are at $\omega_+a/(2\sqrt{2}\pi c)=0.457\pm 0.001$ and $\omega_-a/(2\sqrt{2}\pi c)=0.447\pm 0.001$.

VI. CONCLUSION

We presented an extension of the numerical method of exact eigenvalues and eigenfunctions to solve Maxwell's equations in the presence of woodpile structures. The significant point of this method is the decoupling of the electromagnetic field in each layer: Maxwell's equations are reduced to simple scalar equations and it is then possible to expand the electromagnetic field into the basis of "exact eigenfunctions" associated with the "exact eigenvalues" and it is possible to determine exactly these eigenfunctions and eigenvalues. Moreover, we think that this derivation constitutes a suitable starting point for further analytical estimates of several quantities.

We also presented three checks on our numerical method. We performed a convergence test and checked the reciprocity theorem. These two verifications showed that our numerical method is very efficient. In particular, it requires $\mathcal{N}=3\times 3$ basis functions for an error around 1% for frequencies corresponding to the first band, while 7×7 plane waves are required for the already existing efficient method [22]. This efficiency provides a very important reduction of calculation time and permits us to consider more complicated structures. We benefited from this higher efficiency in an experimental comparison with the silicon woodpile crystal designed for a wavelength of $1.5\ \mu\text{m}$ [12]. We showed that if the structural perturbation observed on the scanning electron microscope image [27] is included in the calculation, excellent agreement with experiments is obtained for wavelengths around the band gap.

Finally, we have studied the possibility to realize a woodpile crystal that has a photonic band gap in the optical range. First, we have shown that the optimal filling ratio is certainly around $f=1.3f_0$, where f_0 is the filling ratio (52) associated with the Bragg condition in one-dimensional systems. Next, we have shown that a photonic band gap opens from an index contrast of 2.05 ± 0.1 . Finally, we have considered more precisely an index contrast of 2.25 corresponding to that of air and Ta_2O_5 : the ideal woodpile structure presents a band gap with a 3.5% relative band gap width; the woodpile with a structural perturbation similar to the experimental realization [12] presents a band gap with a 2.2% relative band gap width.

Moreover, as in the case of the face-centered-cubic lattices of microspheres [16], we think it should be interesting to study woodpile structures made from materials with small absorption. The interest of such materials is that some of them provide a high index contrast. Concerning woodpile structures, the most promising material is certainly silicon

because of the developed fabrication techniques [12] and the small absorption (around 1% in the optical range) that takes place. In order to characterize the properties of such absorptive structures, it is necessary to determine the complex resonances associated with the Helmholtz operator [17] and the generalization of the local density of states [18]. The numerical method we have developed can provide these quantities and we will present their calculation in a forthcoming paper.

ACKNOWLEDGMENTS

We would like to acknowledge Dr. A. Tip for suggesting the integration of the phase to find the complex eigenvalues and for carefully reading the manuscript. We also thank Dr. J. G. Fleming and acknowledge the Sandia National Laboratories' Microelectronics Development Laboratory (MDL) for the fabrication of the silicon photonic lattice. The process and design were guided by Dr. S.-Y. Lin, also of Sandia National Laboratories. This work is part of the research program of the Foundation for Fundamental Research on Matter (FOM) and was made possible by financial support from the Dutch Foundation of Scientific Research (NWO).

APPENDIX A: DETERMINATION OF THE EXACT EIGENVALUES AND EIGENFUNCTIONS

We show here how to determine exactly the eigenvalues and the eigenfunctions of the operator L_1 associated with the first layer in a very general case. An analogous reasoning provides the ones of the operator associated with the others layers, in particular L_2 .

From expression (14), every eigenvalue λ_n of the operator L_1 is either an eigenvalue of L_{ε_1} or L_{μ_1} . So, it is sufficient to determine the set of eigenvalues $\{\lambda_{\nu_1,p}|p\in\mathbb{N}\}$ associated with the set of eigenfunctions $\{\phi_{\nu_1,p}|p\in\mathbb{N}\}$ of the scalar operator L_{ν_1} .

1. The equation satisfied by the exact eigenvalues

From expression (15), the operator L_{ν_1} is the sum of the two operators $\omega^2\varepsilon_1\mu_1+\partial_1\nu_1^{-1}\partial_1\nu_1$ and ∂_2^2 ; the first one is an operator of the single variable x_1 and the second is an operator of the single variable x_2 . Thus, we can perform a variable separation; every eigenfunction of L_{ν_1} can be written as

$$\phi_{\nu_1,p}(x_1,x_2)=\phi_{p_1}^{(1)}(x_1)\phi_{p_2}^{(2)}(x_2), \quad p_1,p_2\in\mathbb{N}, \quad (\text{A1})$$

where $\phi_{p_1}^{(1)}$ and $\phi_{p_2}^{(2)}$ are, respectively, eigenfunctions of the first and second operators that constitute L_{ν_1} .

It is easy to verify that the plane wave

$$\phi_{p_2}^{(2)}(x_2)=\exp\{2i\pi[k_2+q(p_2)]x_2/d_{2,2}\}, \quad q(p_2)\in\mathbb{Z} \quad (\text{A2})$$

is an eigenfunction of the operator ∂_2^2 and satisfies the partial Bloch boundary condition (8) reduced to the variable x_2 . Let $\lambda_{p_2}^{(2)}$ be the associated eigenvalue. Then, from Eq. (A2),

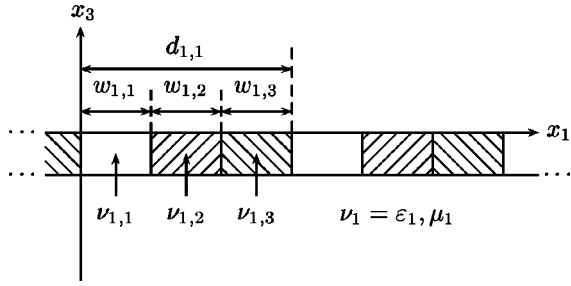


FIG. 15. A layer made of three rods per unit cell ($\mathcal{J}=3$): the three rods have width $w_{1,j}$, permittivity $\varepsilon_{1,j}$, and permeability $\mu_{1,j}$, $j=1,2,3$.

$$\lambda_{p_2}^{(2)} = -\{2\pi[k_2 + q(p_2)]/d_{2,2}\}^2. \quad (\text{A3})$$

Note that, as it is mentioned and used in Sec. III C 1, the eigenfunction $\phi_{\nu_1,p}$ (A1) with the x_2 dependency (A2) is an eigenfunction of the operators ∂_2 and ∂_2^2 : each eigenvalue $ik_{2,n}$ that appears in relation (34) corresponds to an eigenvalue $2i\pi[k_2 + q(p_2)]/d_{2,2}$.

The x_1 dependency of the eigenfunction (A1) is determined using the usual transfer matrix [52–54]. Let $\lambda_{p_1}^{(1)}$ be the eigenvalue associated with $\phi_{p_1}^{(1)}$:

$$[\omega^2 \varepsilon_1 \mu_1 + \partial_1 \nu_1^{-1} \partial_1 \nu_1] \phi_{p_1}^{(1)} = \lambda_{p_1}^{(1)} \phi_{p_1}^{(1)}. \quad (\text{A4})$$

In order to obtain a set of first-order differential equations, we introduce the column vector

$$F_{p_1} = \begin{bmatrix} \nu_1 \phi_{p_1}^{(1)} \\ \nu_1^{-1} \partial_1 \nu_1 \phi_{p_1}^{(1)} \end{bmatrix}. \quad (\text{A5})$$

Note that, from Eq. (A4), the two components of this vector are continuous functions. Now, suppose that the unit cell of the first layer we consider is made of \mathcal{J} rods of width $w_{1,j}$, permittivity $\varepsilon_{1,j}$, and permeability $\mu_{1,j}$, $j=1,2,\dots,\mathcal{J}$ (Fig. 15): we denote by $\nu_{1,j}$ the value of the function ν_1 in the rod j , $j=1,2,\dots,\mathcal{J}$. Then, from Eq. (A4), the vector (A5) satisfies [54]

$$F_{p_1}(d_{1,1}) = T_1(\lambda_{p_1}^{(1)}) F_{p_1}(0), \quad (\text{A6})$$

where

$$T_1(\lambda) = T_{1,\mathcal{J}}(\lambda) T_{1,\mathcal{J}-1}(\lambda) \cdots T_{1,1}(\lambda), \quad (\text{A7a})$$

$$T_{1,j}(\lambda) = P_{1,j}(\lambda, w_{1,j}), \quad (\text{A7b})$$

$$P_{1,j}(\lambda, w) = \begin{bmatrix} \cos(\beta_{1,j} w) & \nu_{1,j} \beta_{1,j}^{-1} \sin(\beta_{1,j} w) \\ -\nu_{1,j}^{-1} \beta_{1,j} \sin(\beta_{1,j} w) & \cos(\beta_{1,j} w) \end{bmatrix}, \quad (\text{A7c})$$

$$\beta_{1,j} = \sqrt{\omega^2 \varepsilon_{1,j} \mu_{1,j} - \lambda}, \quad j=1,2,\dots,\mathcal{J}. \quad (\text{A7d})$$

Note that the four elements of each matrix $T_{1,j}$ only depend on $\beta_{1,j}^2$; expression (A7c) is independent of the definition of

the square root (A7d). In addition to (A6), vector (A5) has to satisfy the partial Bloch boundary condition (8) reduced to the variable x_1

$$F_{p_1}(d_{1,1}) = \exp(2i\pi k_1) F_{p_1}(0). \quad (\text{A8})$$

The combination of (A6) and (A8) implies that $\exp(2i\pi k_1)$ is an eigenvalue of the matrix $T_1(\lambda_{p_1}^{(1)})$; the equation

$$\det[T_1(\lambda_{p_1}^{(1)}) - \exp(2i\pi k_1)] = 0 \quad (\text{A9})$$

determines the eigenvalues $\lambda_{p_1}^{(1)}$. This last equation can be simplified using the fact that $\det T_1 = 1$ [since, from Eq. (A7b), $\det T_{1,j} = 1$, $j=1,2,\dots,\mathcal{J}$]; if $\exp(2i\pi k_1)$ is an eigenvalue of T_1 , then $\exp(-2i\pi k_1)$ is also. Thus, Eq. (A9) is equivalent to

$$\text{tr} T_1(\lambda_{p_1}^{(1)}) - 2 \cos(2\pi k_1) = 0, \quad (\text{A10})$$

where $\text{tr} T_1$ is the trace of matrix T_1 . Once the eigenvalues $\lambda_{p_1}^{(1)}$ are determined from Eq. (A10), the associated eigenvectors $\phi_{p_1}^{(1)}$ are also obtained using the transfer matrix [53]: first, the eigenvector $F_{p_1}(0)$ in \mathbb{C}^2 [associated with the eigenvalue $\exp(2i\pi k_1)$] of the matrix $T_1(\lambda_{p_1}^{(1)})$ is determined; second, the expression of $\phi_{p_1}^{(1)}$ in the rod j can be deduced from

$$F_{p_1}(x_1) = P_{1,j}(\lambda_{p_1}^{(1)}, x_1 - x_{1,j}) F_{p_1}(x_{1,j-1}), \quad (\text{A11})$$

where

$$x_{1,0} = 0, \quad x_{1,j} = \sum_{q=1}^j w_{1,q}, \quad j=1,2,\dots,\mathcal{J}. \quad (\text{A12})$$

Finally, the eigenvalues of the operator L_{ν_1} are

$$\lambda_{\nu_1,p} = \lambda_{p_1}^{(1)} + \lambda_{p_2}^{(2)}, \quad (\text{A13})$$

whose two parts are, respectively, given by Eqs. (A10) and (A3), and the expression of associated eigenvectors is Eq. (A11), whose two parts are, respectively, given by Eqs. (A11) and (A2). Concerning the functions ψ_n (32) used in Sec. III C 1, they are equal to the functions

$$\psi_{\nu_1,p}(x_1, x_2) = (\nu_1^{-1} \partial_1 \nu_1 \phi_{p_1}^{(1)})(x_1) \phi_{p_2}^{(2)}(x_2), \quad (\text{A14})$$

where p_1 and p_2 are in \mathbb{N} , the expression of $\nu_1^{-1} \partial_1 \nu_1 \phi_{p_1}^{(1)}$ in the rod j can be deduced from Eq. (A11) and the expression of $\phi_{p_2}^{(2)}$ is given by Eq. (A2).

2. Numerical determination of the real eigenvalues

Here, we suppose that the permittivity and permeability satisfy the hypothesis (2); the operator L_{ν_1} is self-adjoint and its eigenvalues are then real. The only difficulty in the numerical determination of the eigenvalues (A13) is to find the real numbers $\lambda_{p_1}^{(1)}$ which satisfy the transcendental Eq. (A10).

Since the numbers $\lambda_{p_1}^{(1)}$ are eigenvalues of the operator $\omega^2 \varepsilon_1 \mu_1 + \partial_1 \nu_1^{-1} \partial_1 \nu_1 \leq \omega^2 \varepsilon_+ \mu_+$, these numbers are on the semiaxis $(-\infty, \omega^2 \varepsilon_+ \mu_+]$. This property makes their numerical determination easier. However, two difficulties can occur in this numerical determination. We give herein the solutions we have adopted.

The first difficulty comes from the possibility for two consecutive numbers $\lambda_{p_1}^{(1)}$ to be very close to each other. Our solution is to use an algorithm that determines the zeros of the function $\text{tr} T_1(\lambda) - 2 \cos(2\pi k_1)$ on the left side of Eq. (A10) by taking into account this function together with its derivative with respect to λ . If two numbers $\lambda_{p_1}^{(1)}$ are very close to each other, then the derivative is close to zero. Thus, such algorithm needs to determine the function

$$\frac{d}{d\lambda} [\text{tr} T_1(\lambda) - 2 \cos(2\pi k_1)] = \text{tr} \frac{dT_1}{d\lambda}(\lambda). \quad (\text{A15})$$

The expression of the derivative of the matrix T_1 can be deduced from Eq. (A7):

$$\begin{aligned} \frac{dT_1}{d\lambda} = & \frac{dT_{1,\mathcal{J}}}{d\lambda} T_{1,\mathcal{J}-1} \cdots T_{1,1} + T_{1,\mathcal{J}} \frac{dT_{1,\mathcal{J}-1}}{d\lambda} \cdots T_{1,1} + \cdots \\ & + T_{1,\mathcal{J}} T_{1,\mathcal{J}-1} \cdots \frac{dT_{1,1}}{d\lambda}, \end{aligned} \quad (\text{A16})$$

where, for $j=1,2,\dots,\mathcal{J}$,

$$\frac{dT_{1,j}}{d\lambda} = \frac{1}{2} \begin{bmatrix} w_{1,j} \beta_{1,j}^{-1} \sin(\beta_{1,j} w_{1,j}) & \nu_{1,j} \beta_{1,j}^{-3} \sin(\beta_{1,j} w_{1,j}) - \nu_{1,j} w_{1,j} \beta_{1,j}^{-2} \cos(\beta_{1,j} w_{1,j}) \\ \nu_{1,j}^{-1} \beta_{1,j}^{-1} \sin(\beta_{1,j} w_{1,j}) + \nu_{1,j}^{-1} w_{1,j} \cos(\beta_{1,j} w_{1,j}) & w_{1,j} \beta_{1,j}^{-1} \sin(\beta_{1,j} w_{1,j}) \end{bmatrix}. \quad (\text{A17})$$

The second difficulty comes from the possibility of numerical instabilities in expressions (A7c) and (A17) since the numbers $\beta_{1,j}$ (A7d) can have nonvanishing imaginary part. Our solution is to multiply the four coefficients of matrices $T_{1,j}$ and their derivative (A17) by the number

$$\mathcal{N}_j = \exp[-|\text{Im}(\beta_{1,j})| w_{1,j}], \quad j=1,2,\dots,\mathcal{J} \quad (\text{A18})$$

and the term $2 \cos(2\pi k_1)$ that appears in Eq. (A10) by the product

$$\mathcal{N} = \mathcal{N}_{\mathcal{J}} \mathcal{N}_{\mathcal{J}-1} \cdots \mathcal{N}_1. \quad (\text{A19})$$

3. Numerical determination of the complex eigenvalues

Here, the permittivity and permeability can take any complex value; $\nu_{1,j}$ is in \mathbb{C} , where $\nu_1 = \varepsilon_1, \mu_1$ and $j = 1, 2, \dots, \mathcal{J}$. The operator L_{ν_1} is not self-adjoint and then, its eigenvalues are, in general, in the complex plane. The determination of these complex eigenvalues $\lambda_{p_1}^{(1)}$ that satisfy the Eq. (A10) has been intensively studied using different methods [25,55,56].

We present here a method similar to the one presented in Ref. [55]: the complex eigenvalues are deduced from the real eigenvalues by an analytic continuation. However, our method differs from the one presented in Ref. [55] since we make variation in the phase of the numbers $\nu_{1,j}$ instead of their imaginary part. We think that it is better to make variation in the phase since, from that we have observed, it leaves invariant the generalization to the complex case

$$\text{Re}(\lambda_{\nu_1,1}) \geq \text{Re}(\lambda_{\nu_1,2}) \cdots \geq \text{Re}(\lambda_{\nu_1,p}) \cdots \quad (\text{A20})$$

of numbering (37).

We define for all t in $[0,1]$ the functions

$$\tilde{\nu}_{1,j}(t) = |\nu_{1,j}| \exp[it \arg(\nu_{1,j})], \quad (\text{A21})$$

where $\arg(\nu_{1,j})$ is the phase of the complex number $\nu_{1,j}$, $\nu_1 = \varepsilon_1, \mu_1$, and $j=1,2,\dots,\mathcal{J}$. Substituting the numbers $\nu_{1,j}$ (where $\nu_1 = \varepsilon_1, \mu_1$) for $\tilde{\nu}_{1,j}(t)$ in Eq. (A7), we obtain the matrix $\tilde{T}_1(\lambda, t)$. For each value of t , we define the numbers $\tilde{\lambda}_{p_1}^{(1)}(t)$ that satisfy

$$\text{tr} \tilde{T}_1[\tilde{\lambda}_{p_1}^{(1)}(t), t] - 2 \cos(2\pi k_1) = 0. \quad (\text{A22})$$

Then, the numbers $\tilde{\lambda}_{p_1}^{(1)}(1)$ are the desired complex eigenvalues $\lambda_{p_1}^{(1)}$ and the numbers $\tilde{\lambda}_{p_1}^{(1)}(0)$ are real eigenvalues which can be determined using the method presented in Sec. A2. Assuming that $\tilde{\lambda}_{p_1}^{(1)}(t)$ are continuous and differentiable functions of t , the complex numbers $\tilde{\lambda}_{p_1}^{(1)}(1)$ can be estimated from the numbers $\tilde{\lambda}_{p_1}^{(1)}(0)$ by a numerical integration [55] of

$$\frac{d\tilde{\lambda}_{p_1}^{(1)}}{dt}(t) = - \frac{\text{tr}(\partial \tilde{T}_1 / \partial \lambda)[\tilde{\lambda}_{p_1}^{(1)}(t), t]}{\text{tr}(\partial \tilde{T}_1 / \partial t)[\tilde{\lambda}_{p_1}^{(1)}(t), t]}, \quad (\text{A23})$$

where $\partial \tilde{T}_1 / \partial \lambda$ is given by substituting the numbers $\nu_{1,j}$ for $\tilde{\nu}_{1,j}(t)$ in Eqs. (A16) and (A17), and $\partial \tilde{T}_1 / \partial t$ is determined similarly. Finally, the obtained estimates of numbers $\tilde{\lambda}_{p_1}^{(1)}(1)$ are used to initiate any of the classical methods for the numerical solution of equations [55]. Then, one obtains the desired complex eigenvalues.

In order to eliminate the numerical instabilities, one has to multiply each matrix $T_{1,j}$ and their derivatives by the numbers \mathcal{N}_j (A18) as in Sec. A2.

4. Numerical determination of the eigenfunctions

From Eq. (A11), the expression of each eigenfunction $\phi_{p_1}^{(1)}$ is given by the coefficients of the column vectors $F_{p_1}(x_{1,j})$, $j=0,1,\dots,\mathcal{J}$. On the numerical side, the only difficulty comes from the fact that numerical instabilities in the expression of the transfer matrices (A7b) and (A7c). A solution based on the R -matrix algorithm (or S -matrix) should consist in using the algorithm presented in Ref. [36] to obtain the vector $F_{p_1}(x_{1,0})$ [and the vector $F_{p_1}(x_{1,\mathcal{J}}) = \exp(2i\pi k_1)F_{p_1}(x_{1,0})$] and then, the algorithm presented in Ref. [31 Sec. V] to obtain the vectors $F_{p_1}(x_{1,j})$, $j=1,2,\dots,\mathcal{J}-1$. However, we propose to use another solution that benefits from the fact that we deal with 2×2 matrices.

We define the following complex coefficients:

$$\begin{bmatrix} \mathcal{T}_{11}^j & \mathcal{T}_{12}^j \\ \mathcal{T}_{21}^j & \mathcal{T}_{22}^j \end{bmatrix} = T_{1,\mathcal{J}}(\lambda_{p_1}^{(1)})T_{1,\mathcal{J}-1}(\lambda_{p_1}^{(1)}) \cdots T_{1,j}(\lambda_{p_1}^{(1)}), \quad (\text{A24a})$$

$$\begin{bmatrix} \tau_{11}^j & \tau_{12}^j \\ \tau_{21}^j & \tau_{22}^j \end{bmatrix} = T_{1,j}(\lambda_{p_1}^{(1)})T_{1,j-1}(\lambda_{p_1}^{(1)}) \cdots T_{1,1}(\lambda_{p_1}^{(1)}), \quad (\text{A24b})$$

$$\begin{bmatrix} \mathcal{F}_1^j \\ \mathcal{F}_2^j \end{bmatrix} = F_{p_1}(x_{1,j}), \quad j=0,1,\dots,\mathcal{J}. \quad (\text{A24c})$$

Since $F_{p_1}(x_{1,0})$ is an eigenvector of the matrix $T_1(\lambda_{p_1}^{(1)})$ associated with the eigenvalue $\exp(2i\pi k_1)$, its coefficients satisfy

$$\mathcal{F}_2^0 = -\frac{\mathcal{T}_{11}^{\mathcal{J}}\mathcal{N} - \exp(2i\pi k_1)\mathcal{N}}{\mathcal{T}_{12}^{\mathcal{J}}\mathcal{N}}\mathcal{F}_1^0, \quad (\text{A25})$$

where the numbers $\mathcal{T}_{11}^{\mathcal{J}}\mathcal{N}$ and $\mathcal{T}_{12}^{\mathcal{J}}\mathcal{N}$ are obtained by multiplying each coefficient of matrices $T_{1,j}(\lambda_{p_1}^{(1)})$ by the number

\mathcal{N}_j . The coefficients $\mathcal{F}_1^{\mathcal{J}}$ and $\mathcal{F}_2^{\mathcal{J}}$ are deduced from Eqs. (A8) and (A25) and then, one can obtain the other coefficients for $j=1,2,\dots,\mathcal{J}-1$:

$$\mathcal{F}_1^j = \frac{\mathcal{T}_{22}^{j+1}\tau_{11}^j\mathcal{N}}{\mathcal{T}_{21}^{j+1}\tau_{11}^j\mathcal{N} + \tau_{21}^j\mathcal{T}_{22}^{j+1}\mathcal{N}} \left(\mathcal{F}_2^{\mathcal{J}}\mathcal{T}_{22}^{j+1} - \frac{\mathcal{F}_2^0}{\tau_{11}^j} \right),$$

$$\mathcal{F}_2^j = \frac{\mathcal{T}_{11}^{j+1}\tau_{22}^j\mathcal{N}}{\mathcal{T}_{11}^{j+1}\tau_{12}^j\mathcal{N} + \tau_{22}^j\mathcal{T}_{12}^{j+1}\mathcal{N}} \left(\frac{\mathcal{F}_1^{\mathcal{J}}}{\mathcal{T}_{11}^{j+1}} - \frac{\mathcal{F}_1^0}{\tau_{22}^j} \right), \quad (\text{A26})$$

where, as in Eq. (A25), the multiplication by the number \mathcal{N} consists in multiplying each coefficient of matrices $T_{1,j}(\lambda_{p_1}^{(1)})$ by the number \mathcal{N}_j .

Finally, we have to normalize these functions in order to obtain relation (33). From the definition of the inner product (17), we have to compute

$$\|\phi_{p_1}^{(1)}\|_{v_1}^2 = \frac{1}{d_{1,1}} \int_0^{d_{1,1}} |\phi_{p_1}^{(1)}(x_1)|^2 v_1(x_1) dx_1, \quad (\text{A27})$$

when the functions ε and μ have property (2). In the general case (where ε and μ are complex valued functions), one has to use the formalism presented in Ref. [26] [Sec. 2.3]. It is possible to compute analytically expression (A27):

$$\|\phi_{p_1}^{(1)}\|_{v_1}^2 = \frac{1}{2d_{1,1}} \sum_{j=1}^{\mathcal{J}} \frac{w_{1,j}}{v_{1,j}} (|\mathcal{F}_1^{j-1}|^2 + \beta_{1,j}^{-2} v_{1,j}^{-2} |\mathcal{F}_2^{j-1}|^2) - \beta_{1,j}^{-2} \text{Re}(i\overline{\mathcal{F}_1^{j-1}}\mathcal{F}_2^{j-1} - i\overline{\mathcal{F}_1^j}\mathcal{F}_2^j). \quad (\text{A28})$$

This expression allows to eliminate the numerical instabilities that can occur from the exponential functions. Note that all the coefficients of matrices defined in Sec. III C [Eqs. (39), (40), and (46)] can be also computed analytically in order to eliminate the numerical instabilities.

-
- [1] V.P. Bykov, *Sov. J. Quantum Electron.* **4**, 861 (1975).
[2] E. Yablonovitch, *Phys. Rev. Lett.* **58**, 2059 (1987).
[3] E. Yablonovitch, T.J. Gmitter, and K.M. Leung, *Phys. Rev. Lett.* **67**, 2295 (1991).
[4] J. Joannopoulos, R. Meade, and J. Winn, *Photonic Crystals* (Princeton University Press, Princeton, 1995).
[5] R. Sprik, B.A. van Tiggelen, and A. Lagendijk, *Europhys. Lett.* **35**, 265 (1996).
[6] A. Tip, *Phys. Rev. A* **56**, 5022 (1997).
[7] W.B. Russel, D.A. Saville, and W.R. Schowalter, *Colloidal Dispersions* (Cambridge University Press, Cambridge, 1995).
[8] A. van Blaaderen, R. Ruel, and P. Wiltzius, *Nature (London)* **385**, 321 (1997).
[9] A. Blanco *et al.*, *Nature (London)* **405**, 437 (2000).
[10] Y.A. Vlasov, X.-Z. Bo, J.C. Sturm, and D.J. Norris, *Nature (London)* **414**, 289 (2001).
[11] S.Y. Lin, J.G. Fleming, D.L. Hetherington, B.K. Smith, R. Biswas, K.M. Ho, M.M. Sigalas, W. Zubrzycki, S.R. Kurtz, and J. Bur, *Nature (London)* **394**, 351 (1998).
[12] J.G. Fleming and S.-Y. Lin, *Opt. Lett.* **64**, 49 (1999).
[13] S. Noda, K. Tomoda, N. Yamamoto, and A. Chutinan, *Science* **289**, 604 (2000).
[14] A. Moroz, *Phys. Rev. B* **51**, 2068 (1995).
[15] A. Moroz and C. Sommers, *J. Phys.: Condens. Matter* **11**, 997 (1999).
[16] A. Moroz, *Phys. Rev. Lett.* **83**, 5274 (1999).
[17] A. Tip, A. Moroz, and J.-M. Combes, *J. Phys. A* **33**, 6223 (2000).
[18] A. Tip, *Phys. Rev. A* **57**, 4818 (1998).
[19] K.M. Ho, C.T. Chan, C.M. Soukoulis, R. Biswas, and M. Sigalas, *Solid State Commun.* **89**, 413 (1994).
[20] A. Chutinan and S. Noda, *J. Opt. Soc. Am. B* **16**, 240 (1999).

- [21] V. Lousse, J.-P. Vigneron, X. Bouju, and J.-M. Vigoureux, *Phys. Rev. B* **64**, 201104(R) (2001).
- [22] D.M. Whittaker, *Opt. Lett.* **25**, 779 (2000).
- [23] H.S. Sözüer, J.W. Haus, and R. Inguva, *Phys. Rev. B* **45**, 13 962 (1992).
- [24] L.C. Botten, M.S. Craig, R.C. McPhedran, J.L. Adams, and J.R. Andrewartha, *Opt. Acta* **28**, 413 (1981).
- [25] L.C. Botten, M.S. Craig, and R.C. McPhedran, *Opt. Acta* **28**, 1103 (1981).
- [26] L. Li, *J. Mod. Opt.* **40**, 553 (1993).
- [27] M. J. A. de Dood, B. Gralak, A. Polman, J. G. Fleming, and S. Y. Lin, *Phys. Rev. B* **67**, 035322 (2003).
- [28] K.M. Leung and Y.F. Liu, *Phys. Rev. Lett.* **65**, 2646 (1990).
- [29] Z. Zhang and S. Satpathy, *Phys. Rev. Lett.* **65**, 2650 (1990).
- [30] K.M. Ho, C.T. Chan, and C.M. Soukoulis, *Phys. Rev. Lett.* **65**, 3152 (1990).
- [31] D.M. Whittaker and I.S. Culshaw, *Phys. Rev. B* **60**, 2610 (1999).
- [32] P. Lalanne, *Phys. Rev. B* **58**, 9801 (1998).
- [33] H. van der Lem and A. Moroz, *J. Opt. A, Pure Appl. Opt.* **2**, 395 (2000).
- [34] S. Enoch, R.C. McPhedran, N.A. Nicorovici, L.C. Botten, and J.N. Nixon, *J. Math. Phys.* **42**, 5859 (2001).
- [35] A. Modinos, N. Stefanou, and V. Yannopoulos, *Opt. Express* **8**, 197 (2001).
- [36] B. Gralak, S. Enoch, and G. Tayeb, *J. Opt. Soc. Am. A* **19**, 1547 (2002).
- [37] *Electromagnetic Theory of Gratings*, edited by R. Petit, (Springer-Verlag, Berlin, 1980).
- [38] H. Rigneault, F. Lemarchand, A. Sentenac, and H. Giovannini, *J. Opt. A, Pure Appl. Opt.* **1**, 507 (1999).
- [39] L. Li, *J. Opt. Soc. Am. A* **13**, 1024 (1996).
- [40] L. Li, *J. Opt. Soc. Am. A* **13**, 1870 (1996).
- [41] D. Maystre, *Electromagnetic Theory of Gratings* (Springer-Verlag, Berlin, 1980), Chap. 3.
- [42] E. Popov and M. Nevière, *J. Opt. Soc. Am. A* **17**, 1773 (2000).
- [43] E. Popov and M. Nevière, *J. Opt. Soc. Am. A* **18**, 2886 (2001).
- [44] L. Li, *J. Opt. Soc. Am. A* **14**, 2758 (1997).
- [45] L. Li, *J. Opt. A, Pure Appl. Opt.* **1**, 531 (1999).
- [46] M. Reed and B. Simon, *Methods of Modern Mathematical Physics*, Functional Analysis Vol. I (Academic, New York, 1972).
- [47] M. Reed and B. Simon, *Methods of Modern Mathematical Physics*, Fourier Analysis, Self-Adjointness Vol. II (Academic, New York, 1975).
- [48] M. Reed and B. Simon, *Methods of Modern Mathematical Physics*, Scattering Theory Vol. III (Academic, New York, 1979).
- [49] E.D. Palik, *Handbook of Optical Constants of Solids* (Academic, Boston, 1991), Vol. 2.
- [50] J.Y. Suratteau, M. Cadilhac, and R. Petit, *J. Opt.* **14**, 273 (1983).
- [51] H. Rigneault, S. Robert, C. Begon, B. Jacquier, and P. Moretti, *Phys. Rev. A* **55**, 1497 (1997).
- [52] M. Reed and B. Simon, *Methods of Modern Mathematical Physics*, Analysis of Operators Vol. IV (Academic, New York, 1978).
- [53] A. Figotin and V. Gorenstveig, *Phys. Rev. B* **58**, 180 (1998).
- [54] D. Felbacq, B. Guizal, and F. Zolla, *Opt. Commun.* **152**, 119 (1998).
- [55] G. Tayeb and R. Petit, *Opt. Acta* **31**, 1361 (1984).
- [56] S.-E. Sandström, G. Tayeb, and R. Petit, *J. Electromagnetic Waves Applications* **7**, 631 (1993).